

# Probing classical and quantum-mechanical baths with a qubit

by  
Thomas Fink

**Master's Thesis in Physics**

presented to

**The Faculty of Mathematics, Computer Science and Natural Sciences  
at RWTH Aachen University**

Department of Physics, Institute II C

December 2012

supervised by

Prof. Hendrik Bluhm, PhD  
Prof. Dr. Barbara Terhal



## **Abstract**

Extending coherence times to allow for qubit manipulation is at the heart of quantum information research. The investigation of the deleterious interactions between the qubit and its environment is thus of paramount importance. In this thesis, techniques using qubit evolution and readout to investigate interactions with both classical and quantum-mechanical noise baths are introduced. Simulations to predict the usability of these methods in electrically confined GaAs electron spin qubits and superconducting qubits are shown.



---

# Contents

<b>I</b>	<b>Introduction</b>	<b>1</b>
<b>1</b>	<b>Motivation</b>	<b>3</b>
<b>2</b>	<b>Quantum information</b>	<b>5</b>
2.1	Qubit . . . . .	5
2.1.1	Bloch sphere . . . . .	6
2.1.2	Electron spin qubit . . . . .	7
2.1.3	Superconducting qubit . . . . .	9
2.2	Coherence times . . . . .	10
2.2.1	Energy relaxation time . . . . .	10
2.2.2	Dephasing time . . . . .	10
2.2.3	Inhomogeneous broadening time . . . . .	11
2.3	Pulse sequences . . . . .	11
<b>II</b>	<b>Noise spectroscopy</b>	<b>13</b>
<b>3</b>	<b>Motivation</b>	<b>15</b>
<b>4</b>	<b>Theory</b>	<b>17</b>
4.1	Hamiltonian . . . . .	17
4.2	Noise sources . . . . .	17
4.2.1	Nuclear spin bath . . . . .	18
4.2.2	1/f noise . . . . .	20
<b>5</b>	<b>Measurement scheme</b>	<b>23</b>
<b>6</b>	<b>Correlation function</b>	<b>25</b>
<b>7</b>	<b>Simulations</b>	<b>31</b>
7.1	Lorentzian . . . . .	31
7.1.1	One Lorentzian . . . . .	31
7.1.2	Two Lorentzians . . . . .	33

7.2 Nuclear spin bath . . . . .	34
7.3 1/f noise . . . . .	38
<b>8 Summary</b>	<b>41</b>
 <b>III Probing quantum-mechanics in a spin bath</b>	 <b>43</b>
<b>9 Motivation</b>	<b>45</b>
<b>10 Theory</b>	<b>47</b>
10.1 Central spin problem . . . . .	47
10.2 Hamiltonian . . . . .	48
<b>11 Measurement scheme</b>	<b>51</b>
11.1 Toy model scheme . . . . .	54
11.2 Pulse scheme . . . . .	55
<b>12 Calculation of correlation function</b>	<b>57</b>
12.1 Toy model scheme . . . . .	57
12.1.1 Semiclassical approach . . . . .	57
12.1.2 Quantum-mechanical approach . . . . .	61
12.2 Pulse scheme . . . . .	63
<b>13 Simulations</b>	<b>67</b>
13.1 Toy model scheme . . . . .	67
13.2 Pulse scheme . . . . .	69
<b>14 Summary</b>	<b>73</b>
 <b>IV Conclusion</b>	 <b>75</b>
<b>15 Conclusion</b>	<b>77</b>
<b>Appendix</b>	<b>I</b>
<b>Bibliography</b>	<b>III</b>
<b>List of Figures</b>	<b>IX</b>

# Part I

---

## Introduction





## Motivation

Over the past few decades, research on the manipulation and readout of individual quantum-mechanical systems has gathered an enormous pace for its potential use for computation, culminating in this year's Nobel prize in physics [1]. Quantum computation may be considered crucial for two different sets of problems. First, the design and individual control of quantum-mechanical systems enables the experimenter to construct an easily controllable replica of another quantum-mechanical system. Though it might not always be possible to get an exact copy of the original system, careful design of this replica allows to include the dominant interactions, i.e. an effective Hamiltonian that covers the most important properties [2]. This system may then be used to simulate and study the behavior of the original system. An example where quantum computation may tremendously promote investigations are many-body systems such as high-temperature superconductors. Due to the excessively large number of quantum-mechanically interacting particles, these systems are not tractable today but may be studied using a quantum simulator [3]. The example illustrates that using a quantum system to simulate another is actually a very natural choice and the idea was already put forward by Richard Feynman in 1982 [4]. However, the level of control over a single quantum-mechanical system required becomes only feasible today. For an overview on recent experimental progress in this field see Ref. [5]. The second application relies on performing algorithms with controllable quantum-mechanical systems. For several problems, such as prime number factorization [6], searching for one element in a large database [7], and solving linear equations [8], the computation has been shown to be efficient when algorithms based on quantum-mechanical systems are used. This allows the calculation of problems that are intractable with classical computers. The combination of the required control of individual quantum-mechanical systems and the two main prospects where quantum computation may lead to ground-breaking insights make the realization of these systems both a highly challenging and rewarding goal.

In this thesis, I will focus on the interactions of a quantum-mechanical two-level system, a so-called *quantum bit*, with the surrounding environment. When such systems are used for computation, i.e. for storing and processing information, interactions with their environment lead to unwanted diffusion of the stored information. Understanding these processes

is thus crucial for the development of techniques to mitigate the loss of information. Part [I](#) of the thesis will be dedicated to an introduction into the main concepts of quantum information necessary for the comprehension of the remainder. In Part [II](#), I will investigate how a quantum-mechanical two-level system can be used to extract information about a surrounding classical noise bath. A technique to investigate the associated noise bath spectrum via projective measurements of a coupled two-level system will be presented and simulations exhibiting the usefulness of this method for two prominent realizations of those systems (based on electron spins and superconducting circuits) are shown. In Part [III](#) of the thesis, I will investigate the coupling of a two-level system, i.e. an electron spin, to a fluctuating bath of nuclear spins. In contrast to the previous part, the bath will be treated quantum-mechanically and a measurement scheme to detect backaction from the two-level system on the noise bath will be introduced. Simulations showing that this interaction leads to a measurable effect are shown. This part also aims at testing the assumption of a classical noise bath made in the previous part and sheds light on the effect of noncommuting measurements. Part [IV](#) will briefly summarize the main results and give an outlook on future directions.

# Quantum information

In this chapter I will give a brief introduction into the main concepts of quantum information necessary for the remainder of the thesis to be comprehensible. For an exhaustive review on quantum information theory the reader is referred to Ref. [9].

## 2.1 Qubit

A quantum bit (qubit) is the quantum-mechanical analogon of a regular bit used for classical information encoding. While the latter is a digital system that can either be in its states 0 or 1, a qubit's state exists in a two-dimensional Hilbert space and may consist of superpositions of its two basis states  $|0\rangle$  and  $|1\rangle$ . It can thus be regarded as the analog, quantum-mechanical counterpart of a classical bit.

The most generic representation of a qubit state is given by

$$|\psi\rangle = \alpha|0\rangle + \beta|1\rangle \quad (2.1)$$

where  $\alpha, \beta \in \mathbb{C}$  fulfill the normalization condition  $|\alpha|^2 + |\beta|^2 = 1$ . In principle, any quantum-mechanical two-level system such as an electron spin, the ground and excited state of an atom or the polarization of a photon may be regarded as a qubit. However, five criteria have been identified in order to use a qubit for quantum computation: scalability, the ability to initialize a desired state, sufficiently long coherence times compared to the gate operation time, a universal set of quantum gates and the ability to measure the qubit state [10]. Moreover, two additional criteria have been introduced to enable quantum communication between qubits and thus quantum information processing: the ability to interconvert stationary and flying qubits and the ability to transmit flying qubits between specified locations [11].

In this thesis, I will consider two very prominent realizations of a qubit: electron spin and superconducting qubits. The latter will, however, be introduced only very briefly as the focus for the major part of the thesis will lie on electron spin qubits.

### 2.1.1 Bloch sphere

The isomorphism of the Lie algebras  $su(2)$  and  $so(3)$  gives rise to a very simple representation of a qubit state as a three-dimensional vector in a unit sphere. The state in Eq. 2.1 can be rewritten as

$$\begin{aligned} |\psi\rangle &= e^{i\gamma} \left( \cos\left(\frac{\theta}{2}\right) |0\rangle + e^{i\phi} \sin\left(\frac{\theta}{2}\right) |1\rangle \right) \\ &\rightarrow \cos\left(\frac{\theta}{2}\right) |0\rangle + e^{i\phi} \sin\left(\frac{\theta}{2}\right) |1\rangle. \end{aligned} \quad (2.2)$$

Note that the global phase  $\gamma$  is not observable experimentally and is thus neglected in the second step. The angles  $\theta$  and  $\phi$  define a unique point on a unit sphere which is called Bloch sphere. This geometric representation is depicted in Fig. 2.1. In addition to

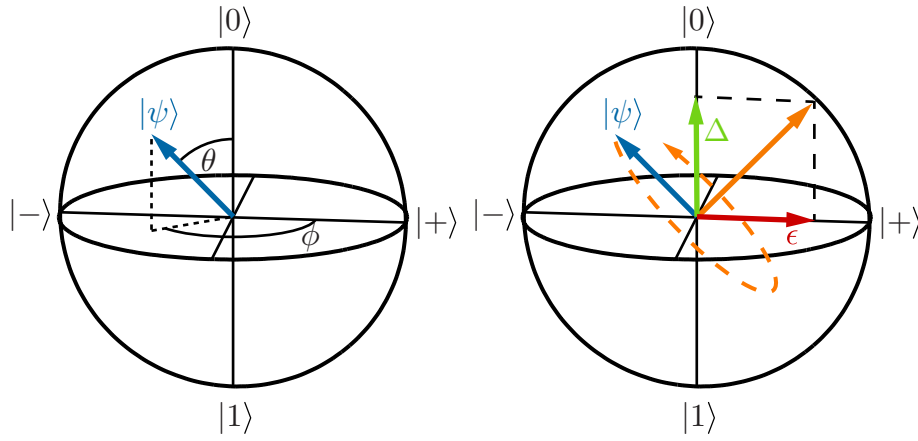


**Figure 2.1:** Visualization of a state  $|\psi\rangle$  defined by its angles  $\theta$  and  $\phi$  on a Bloch sphere (left).  $|\pm\rangle = (|0\rangle \pm |1\rangle)/\sqrt{2}$  represent superposition states. The Hamiltonian in Eq. 2.3 leads to rotations about an axis (orange) defined by  $\epsilon$  and  $\Delta$  with precession rate  $\sqrt{\epsilon^2 + \Delta^2}$  (right).

visualizing a qubit state, unitary single-qubit operations (that is  $U^\dagger U = 1$  where  $U$  is the evolution operator) can also be represented in a Bloch sphere via rotations of the qubit state vector. Consider the following Hamiltonian  $H$  acting on the state  $|\psi\rangle$ :

$$\hat{H} = \frac{\hbar}{2} [\epsilon \hat{\sigma}_x + \Delta \hat{\sigma}_z]. \quad (2.3)$$

In the Bloch sphere representation, the effect of the Pauli matrix  $\hat{\sigma}_x$  ( $\hat{\sigma}_z$ ) corresponds to rotations about the  $x$ -axis ( $z$ -axis) with precession rate  $\epsilon$  ( $\Delta$ ) as depicted in Fig. 2.1. A Hamiltonian of this form enables universal single-qubit operations as rotations about two axes, possibly resulting in a combined, tilted rotation axis (see orange axis in Fig. 2.1), allow for the qubit state to reach every point on the Bloch sphere surface.

### 2.1.2 Electron spin qubit

A natural choice for a quantum-mechanical two-level system is the electron spin which offers both the perspective of a scalable qubit system and sufficiently long coherence times due to weak coupling to its environment (compared to e.g. using the charge of an electron). The qubit basis may be formed by either one electron in a spin up  $|\uparrow\rangle$  and down  $|\downarrow\rangle$  configuration or two electrons in a singlet  $|S\rangle = \frac{1}{\sqrt{2}}(|\uparrow\downarrow\rangle - |\downarrow\uparrow\rangle)$  or triplet  $|T_0\rangle = \frac{1}{\sqrt{2}}(|\uparrow\downarrow\rangle + |\downarrow\uparrow\rangle)$  state. In this thesis, I will focus on the latter as it offers the possibility of all-electrical control and does not necessitate any externally induced magnetic field gradients which is very beneficial for a scalable system. The first experimental realization of an electrically controlled singlet triplet ( $S - T_0$ ) qubit has been shown by Petta *et al.* in 2005 [12] and is depicted in Fig. 2.2. The system consists of a GaAs/Al<sub>0.3</sub>Ga<sub>0.7</sub>As

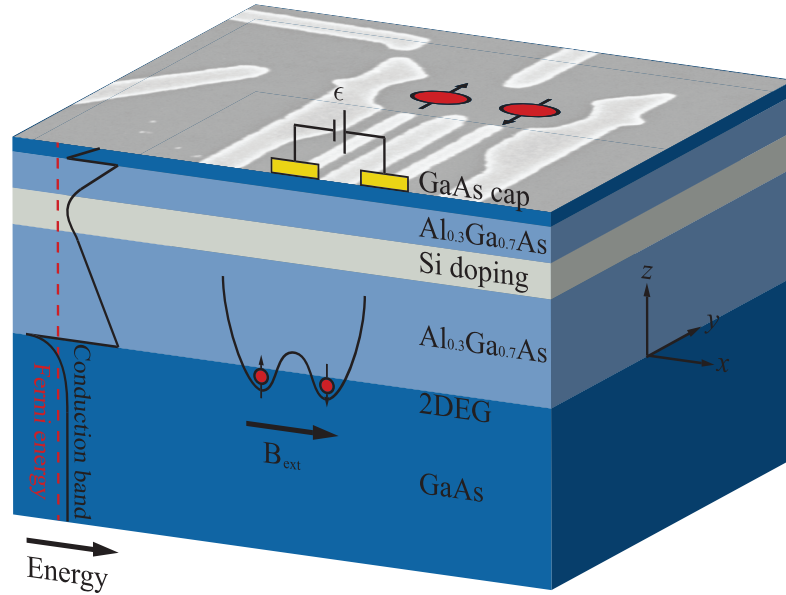


**Figure 2.2:** Schematic of an electrically controlled singlet triplet qubit in a GaAs/Al<sub>0.3</sub>Ga<sub>0.7</sub>As heterostructure. Due to the particular band gap configuration, a two-dimensional electron gas (2DEG) is induced at the interface of GaAs and Al<sub>0.3</sub>Ga<sub>0.7</sub>As. Careful tuning of voltages applied to metal gates on top of the structure depletes the 2DEG underneath and creates a double well potential where each well contains exactly one electron. For details see text. SEM image from Ref. [13].

heterostructure. Due to the larger band gap of the latter, the conduction band is bent below the Fermi energy of the system such that electrons stemming from the Si dopants accumulate at the interface of GaAs and Al<sub>0.3</sub>Ga<sub>0.7</sub>As approximately 100 nm below the surface, forming a two-dimensional electron gas (2DEG). The electrons are confined in the  $z$ -direction but can move freely in the  $x, y$ -plane. Voltages applied to metal gates on

top (white / gold) deplete the electron gas underneath such that a double well potential (double quantum dot) is created. Due to the similar lattice constant of the two materials, no strain is induced. Careful calibration of the voltages applied to the different gates allows for tuning of the double quantum dot such that each dot is occupied by exactly 0, 1 or 2 electrons.

The voltage  $\epsilon$ , which is called *detuning* in this qubit system, controls the relative difference of the energy levels in the left and right dot and thus the transition from the doubly occupied  $(0, 2)$  charge state to the  $(1, 1)$  state. The energy diagram of the system as a function of this parameter is depicted in Fig. 2.3. Due to the tunnel coupling  $t_c$  between the

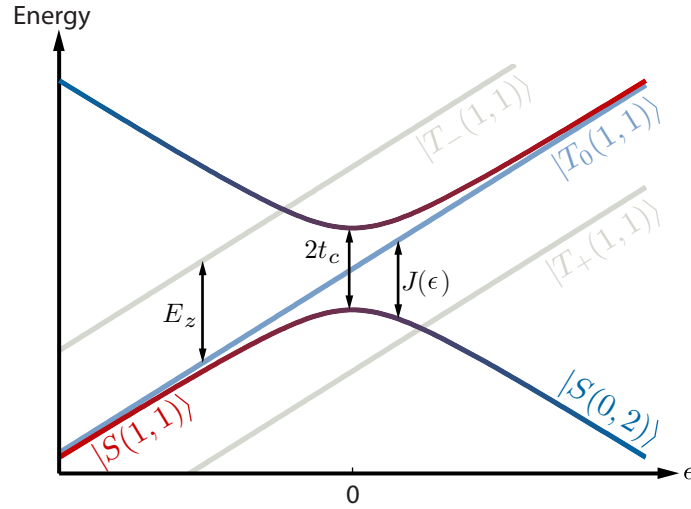


**Figure 2.3:** Energy diagram of a singlet triplet qubit. At  $\epsilon = 0$  an avoided crossing appears due to the tunnel coupling  $t_c$  between the two dots. The  $|T_{\pm}(1, 1)\rangle$  states (grey) are split off by the Zeeman energy  $E_z$  due to an external magnetic field. The color gradient illustrates the transition from the  $(0, 2)$  (dark blue) to the  $(1, 1)$  (red) charge state. At  $\epsilon \ll 0$ ,  $|S(1, 1)\rangle$  and  $|T_0(1, 1)\rangle$  are degenerate.

two dots, an avoided crossing with a magnitude of  $2t_c$  appears at  $\epsilon = 0$ , where this point is defined as the minimum distance between the hybridized states. The exchange energy  $J(\epsilon) \sim e^{\frac{\epsilon}{\epsilon_0}}$  can be illustrated as the energy difference of the  $|S(1, 1)\rangle$  and  $|T_0(1, 1)\rangle$  state. Note, however, that this relationship is purely phenomenological. Due to an external field  $\mathbf{B}_{ext}$  parallel to the 2DEG, the states  $|T_{\pm}(1, 1)\rangle$  are split off from the  $|T_0(1, 1)\rangle$  state by  $\pm g\mu_B B_{ext}$  where  $g = -0.44$  is the electron gyromagnetic factor in GaAs and  $\mu_B$  is Bohr's magneton.

Presence and control of  $J(\epsilon)$  leads to oscillations between the  $|S(1, 1)\rangle$  and  $|T_0(1, 1)\rangle$  state and corresponds to one axis of rotation in the Bloch sphere picture. The second axis of rotation is the difference of the Overhauser field components  $\Delta B^z \parallel \mathbf{B}_{ext}$  that the electrons experience in each respective dot due to their hyperfine coupling to the nuclear spins. This interaction will be reviewed in detail in the following part. At  $\epsilon \ll 0$ , where  $|S(1, 1)\rangle$  and

$|T_0(1, 1)\rangle$  are degenerate, the Hamiltonian for the system in the  $\{|\uparrow\downarrow\rangle, |\downarrow\uparrow\rangle\}$  basis is given by

$$\hat{H} = \frac{1}{2} \begin{pmatrix} g\mu_B \Delta B_z & J(\epsilon) \\ J(\epsilon) & -g\mu_B \Delta B_z \end{pmatrix} = \frac{1}{2} [J(\epsilon)\hat{\sigma}_x + g\mu_B \Delta B_z \hat{\sigma}_z]. \quad (2.4)$$

For a detailed review see Ref. [14]. Comparing this Hamiltonian with Eq. 2.3 reveals that control of the detuning and presence of the nuclear spins allow for universal single-qubit manipulations. Readout of this system is realized by sweeping to  $\epsilon \gg 0$  where due to Pauli blockade no transition to the  $(0, 2)$  charge state occurs only if the system is in the  $|T_0\rangle$  state whereas a charge transport can be measured during the transition  $|S(1, 1)\rangle \rightarrow |S(0, 2)\rangle$  with a nearby sensing dot [15] or a quantum point contact [16, 17].

### 2.1.3 Superconducting qubit

Superconducting circuits are promising candidates due to ease of fabrication of even complex circuit architectures which offers the promise of scalability. There are several concepts on how to realize a qubit with a superconducting circuit. The first realization was the Cooper pair box [18–20] which made use of the states  $|N\rangle$  and  $|N + 1\rangle$  as logical states where  $N$  denotes the number of Cooper pairs in the box formed by a Josephson junction. More advanced concepts, such as the flux, transmon and phase qubit, were developed to each reduce the sensitivity to particular noise channels such as e.g. charge and flux noise. For a detailed review see Ref. [21, 22]. Initialization of these qubits is often realized through energy relaxation which is set by  $T_1$ . This long initialization process may however be circumvented by using a projective measurement to initialize the qubit as demonstrated in Ref. [23]. Manipulation of the qubit can be achieved through the application of microwave pulses while readout is realized with an adjacent and weakly coupled transmission line. The different superconducting qubit systems are all based on the only non-linear element available for operation at low temperatures which are required to maintain superconductivity: the Josephson junction. This element consists of two superconducting electrodes that are separated by a small insulating barrier. This barrier can be realized by e.g. a small layer of oxide between two Aluminum electrodes and acts as an effective non-linear inductivity, shunting the capacitor formed by the two electrodes by tunneling of Cooper pairs. Fig. 2.4 (a) shows a schematic representation of the Josephson junction. This element can be regarded as a non-linear, non-dissipative electrodynamical oscillator [25].

Advanced systems such as the transmon qubit consisting of two Josephson junctions [24], are capable of performing even complex algorithms such as the Toffoli gate. A schematic is illustrated in Fig. 2.4 (b). Their dephasing times lie on the order of  $T_2^* \sim 1 \mu\text{s}$  and are limited by energy relaxation [26]. Combination of superconducting qubits with cavity quantum electrodynamics is a powerful tool to couple the qubit to a resonator and thus

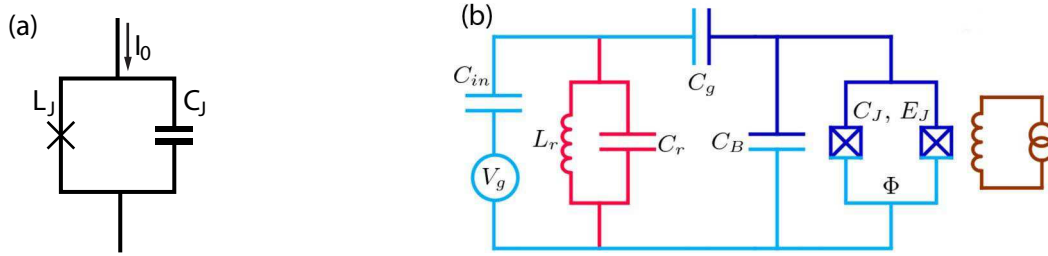


**Figure 2.4:** (a) Schematic representation of the Josephson junction as an effective inductivity  $L_J$  shunting the capacitor  $C_J$  formed by the two electrodes. (b) Circuit diagram of the transmon qubit. Two Josephson junctions with capacitance  $C_J$  and Josephson energy  $E_J$  are shunted by a large capacitance  $C_B$ .  $E_J$  is tuned with a magnetic flux  $\Phi$  applied to the island formed by the two junctions with the brown coil on the right. The capacitively coupled gate voltage  $V_g$  controls the number of Cooper pairs in the junctions. The transmission line, characterized by the inductivity  $L_r$  and capacitance  $C_r$ , is coupled to the Cooper pair box for control and readout of the qubit state [24].

mediate long-range interactions. Lucero et al. showed that they are capable to entangle up to three qubits with a single resonator mode and perform Shor's algorithm on the number 15 which makes these qubits good candidates for building a scalable solid-state quantum computer architecture [27].

## 2.2 Coherence times

To characterize the decay of qubit coherence, three different time scales have been adapted from nuclear magnetic resonance representing the different processes due to which a qubit may lose its information [28].

### 2.2.1 Energy relaxation time $T_1$

The energy relaxation time  $T_1$ , also called longitudinal relaxation time, accounts for processes in which the excited qubit state relaxes to its ground state. In the Bloch sphere picture of Fig. 2.1, this corresponds to relaxation towards the south pole of the sphere as shown in Fig. 2.5. The energy relaxation time is typically much longer than the gate operation time both for singlet triplet qubits [29, 30] and superconducting qubits [31–34].

### 2.2.2 Dephasing time $T_2$

The dephasing time  $T_2$ , also called transverse relaxation time, describes the time scale on which the qubit loses information about its phase or, in other words, how fast a su-



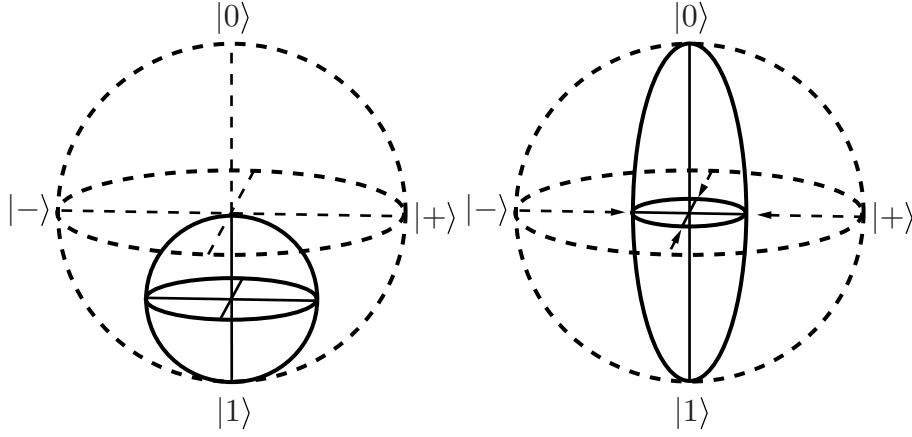


**Figure 2.5:** Visualization of  $T_1$  (left) and  $T_2/T_2^*$  (right) relaxation. The original Bloch sphere (dashed line) is compressed due to the respective decoherence process (solid line).

perposition state (such as  $|S\rangle$  and  $|T_0\rangle$  in the singlet triplet qubit) decays into a mixed state. It includes decoherence stemming from fast, uncorrelated noise compared to the qubit evolution time. Transferring this process onto the Bloch sphere results in shrinking of the sphere in the equatorial plane as shown in Fig. 2.5.

### 2.2.3 Inhomogeneous broadening time $T_2^*$

Inhomogeneous broadening results from ensemble or temporal averaging and stems from inhomogeneities in the initial noise bath configuration. It includes slowly fluctuating noise that is constant for a single qubit evolution time but varies between different cycles that are averaged over. The Bloch sphere representation of this process is identical to that of the  $T_2$  time and shown in Fig. 2.5. It corresponds to shrinking of the Bloch sphere towards the origin which corresponds to a mixed state.

## 2.3 Pulse sequences

In order to mitigate the effects of dephasing, pulse sequences consisting of a series of  $\pi$ -pulses applied to the qubit have been introduced. In the Bloch sphere picture, a  $\pi$ -pulse corresponds to a rotation of  $180^\circ$  about an axis in the equatorial plane. The sequences were partly adapted from NMR, such as Hahn's spin echo [35] and the Carr-Purcell-Meiboom-Gill (CPMG) sequence [36], but also developed directly for extending qubit coherence, e.g. concatenated [37] or Uhrig's dynamical decoupling (UDD) [38]. Effectively, pulse sequences decouple the qubit from noise fluctuating on a specific frequency scale which is determined by the timing and total number of  $\pi$ -pulses applied. To illustrate the

functioning of the sequences, the simplest of all, the spin echo sequence, is depicted in Fig. 2.6. More elaborate sequences typically include a larger number of  $\pi$ -pulses and a

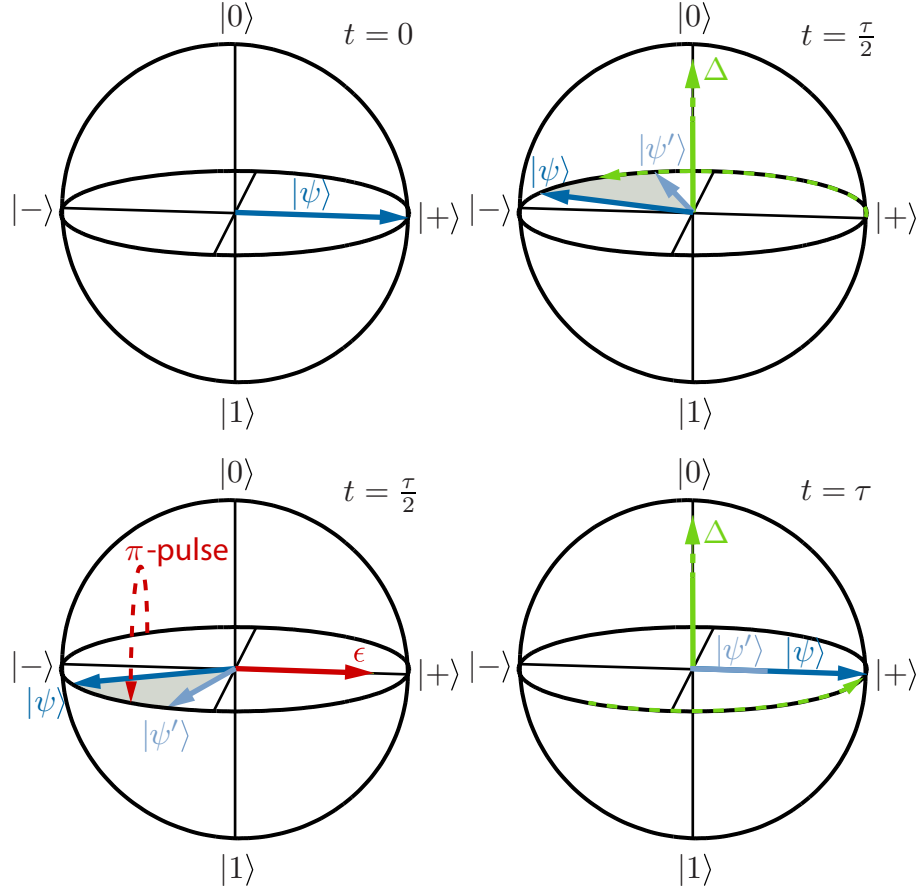


**Figure 2.6:** Schematic of the spin echo sequence. The qubit is initialized at  $t = 0$  in a superposition state  $|+\rangle = (|0\rangle + |1\rangle)/\sqrt{2}$  followed by a free evolution for time  $\frac{\tau}{2}$ . During this time, the qubit state vector  $|\psi\rangle$  precesses about the  $z$ -axis under the influence of the Hamiltonian  $H = \frac{\Delta}{2}\sigma_z$  (indicated by green line). Fluctuations of the parameter  $\Delta$  lead to different precession rates between successive cycles and thus a difference in the amount of precession as indicated by the grey shaded area.  $|\psi\rangle$  (blue) represents a cycle with a larger  $\Delta$  and thus a larger precession rate whereas  $|\psi'\rangle$  (light blue) corresponds to a evolution time when  $\Delta$  is smaller and the state precession is thus slower. When a  $\pi$ -pulse (red) is applied,  $|\psi'\rangle$  is transferred to a position where its total precession is larger than that of  $|\psi\rangle$  and the position of the two states is exchanged. After another free evolution of time  $\frac{\tau}{2}$ , the two states coincide again which is equivalent to refocussing. This perfect refocussing is however only possible if  $\Delta$  fluctuates with frequencies  $\omega \leq 1/\tau$  corresponding to quasi-static noise.

nonlinear distribution of their timing. However, the effect of extending the coherence time by decoupling the qubit from environment fluctuations up to a characteristic frequency is qualitatively similar.

# Part II

---

## Noise spectroscopy



### Motivation

The loss of qubit information is caused by entanglement between the qubit and its environment [39]. In order to mitigate this detrimental effect and thus extend coherence times, understanding the dominating processes coupling the qubit to its environment is crucial. Significant information about these coupling interactions can be deduced from investigating the noise acting on the qubit in the frequency domain, i.e. by measuring the noise spectrum.

Pulse sequences have been shown to be useful in this context: besides significantly increasing coherence times by effectively decoupling the qubit from its environment [13], they can also be used to gain information about the noise's spectral distribution by observing the decay of qubit coherence under the application of a suitable sequence. Cywiński et al. showed that the UDD sequence can be used to obtain the spectrum's moments if Gaussian noise is assumed [40]. In a similar way, Yuge et al. proposed a sequence of equidistant  $\pi$ -pulses to infer the noise spectrum from sweeping the evolution time [41]. However, the decoupling mechanism of pulse sequences is only efficient up to a certain sequence-dependent frequency range which in turn implies that they are only sensitive to the noise spectrum above this frequency. This constraint limits the application of pulse sequence-based spectroscopy: to investigate lower frequency ranges, long evolution times compared to the qubit's dephasing time are required as the frequency range where the pulse sequence is sensitive scales inversely with the total evolution time. This relationship implies that frequency scales much smaller than the inverse dephasing time are inaccessible with pulse sequence-based spectroscopy due to a low measurement contrast. An additional constraint arises from imperfect  $\pi$ -pulses. To achieve longer evolution times and thus lower frequency bounds, a large number of such pulses are needed which might be hampered by accumulating pulse errors. Pulse sequence-based spectroscopy can thus be used to reveal the high-frequency region of the noise spectrum. In Ref. [31] this method has been experimentally realized by applying a CPMG sequence to a superconducting flux qubit resulting in a lower frequency bound of  $\sim 100$  kHz.

The investigation of the low-frequency noise spectrum has been realized with direct measurement of the qubit state. This technique relies on measuring the autocorrelation func-

tion of two initialization-evolution-measurement cycles with a delay time in between. Calculating the Fourier transform leads to the noise spectrum. The frequencies accessible with this method are determined by the averaging necessary for each measurement which limits the repetition time and thus sets an upper bound on the accessible frequency range for ensemble-averaged spectroscopy. This bound is given by  $1/2N_G\Delta t$  where  $N_G$  is the number of cycles that are averaged over and  $\Delta t$  is the repetition time. Typically, it is on the order of 1-10 Hz [29, 42, 43]. Ref. [44] introduced an effective delay time  $\Delta t$  using dynamical decoupling techniques between two free induction decays of a NV centre qubit. Replacing the ensemble-averaging by single-shot readout has been shown to increase this frequency to  $1/2\Delta t \sim 100$  Hz [45]. Ref. [46] proposed the investigation of the noise autocorrelation function by separating it into long-time and short-time correlations investigated via direct and pulse sequence-based spectroscopy, respectively. However, this technique is subject to the same limitations as the approaches before.

Comparing pulse sequence-based and direct spectroscopy a frequency gap of at least three orders of magnitude inaccessible with these method remains for superconducting qubits and similar limitations are likely to occur in electron spin qubits. This region is yet of particular interest for example to investigate whether the ubiquitously observed  $1/f^\alpha$  spectrum indeed prevails over the whole range of frequencies in superconducting qubits or to characterize the assumed cutoff in electron spin qubits [47]. In this part, I will introduce a measurement scheme to investigate the noise bath in the frequency domain to bridge the gap between direct and pulse sequence-based noise spectroscopy. Electrically confined electron spin qubits and superconducting qubits with their respective noise spectra will be considered to show the usability of the presented technique. However, it is important to note that the sequence is universal with respect to the qubit system as long as fast initialization and measurement is ensured. The idea and main results presented in this part can also be found in Ref. [48].

## Theory

### 4.1 Hamiltonian

In this part, pure dephasing is considered implying that the energy relaxation time of the qubit is much longer than the evolution time of interest. This assumption has been shown to be adequate in a range of experiments on electron spins where  $T_1 \sim 16 \mu\text{s}$  at  $B_{ext} = 0 \text{ T}$  [29] up to  $T_1 > 1 \text{ s}$  at  $B_{ext} = 1 \text{ T}$  [30] as well as superconducting qubits [31–34] in off-sweet spot operations. The noise bath is modeled as a classical, Gaussian noise variable  $\beta(t)$  which fluctuates around zero with a variance  $\langle \beta^2 \rangle$

$$\hat{H} = \frac{\hbar}{2} [\Omega + \beta(t)] \hat{\sigma}_z \quad (4.1)$$

where  $\Omega$  is the qubit energy splitting [40]. Eq. 4.1 implies that a classical noise spectrum

$$S(\omega) = \int_{-\infty}^{\infty} e^{i\omega\delta t} \langle \beta(t)\beta(t+\delta t) \rangle d\delta t \quad (4.2)$$

with the noise autocorrelation function  $\langle \beta(t)\beta(t+\delta t) \rangle$  can be associated to the environment of the qubit and that backaction from the qubit on the noise bath is negligible. The validity of this approach is not clear a priori as it neglects the noise bath's quantum-mechanical nature and will thus be discussed when the different noise sources are introduced. In this part, this semi-classical model is adopted in order to investigate and determine the spectral distribution of the noise bath under this assumption. Failure of the model to describe experimental results might indicate that neglecting the bath's quantum-mechanical properties is not sufficient.

### 4.2 Noise sources

In this section, I will introduce the dephasing noise processes predominant in singlet triplet and superconducting qubits and also motivate the spectrum used for the simulations. Again, emphasis will be placed on the former qubit system.

### 4.2.1 Nuclear spin bath

In the GaAs singlet triplet qubit, the electron spin is coupled to  $\sim 10^6$  nuclear spins [49] through the hyperfine interaction

$$\hat{H}_{hf} = \sum_{d,i} A_i \vec{J}_i \cdot \vec{S}_d \quad (4.3)$$

as depicted in Fig. 4.1. The index  $d = L, R$  labels the left and right dot, respectively,

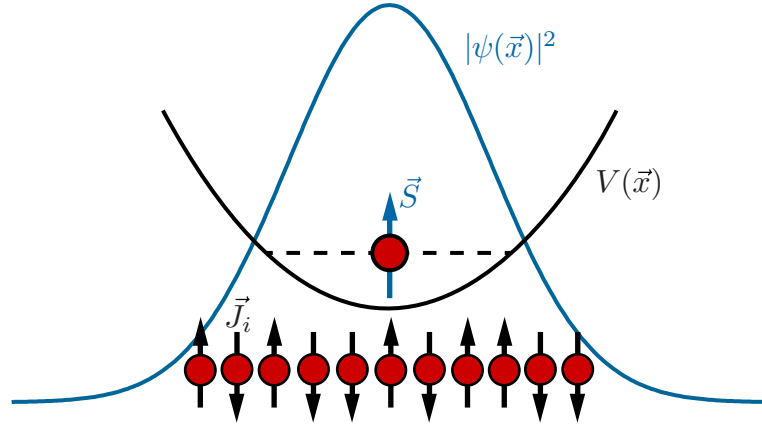


**Figure 4.1:** Schematic of the coupling between the electron spin  $\vec{S}$  (blue) and the surrounding nuclear spins  $\vec{J}_i$ . The electron wave function  $|\psi(\vec{x})|^2$  is determined by the electrostatic confinement potential  $V(\vec{x})$  creating a ground state (dashed line) occupied by one electron.

and the sum runs over all nuclear spins  $\vec{J}_i$  coupled to the electron spin  $\vec{S}_d$  in dot  $d$ . This scenario, consisting of a single spin coupled to a bath comprising other spins, is renowned as the central spin problem and has gained both experimental and theoretical interest to investigate the underlying physical properties and also for possible application in quantum information. It will be reviewed in detail in the following part. The hyperfine energy

$$A_{d,i} = \mathcal{A}_{\alpha(i)} |\psi_{d,i}|^2 \quad (4.4)$$

is given in terms of a species-dependent hyperfine energy  $\mathcal{A}_{\alpha(i)}$  where  $\alpha(i)$  denotes the different isotopes  $^{69}\text{Ga}$ ,  $^{71}\text{Ga}$  and  $^{75}\text{As}$  present in the quantum dot [50] and  $|\psi_{d,i}|^2$ , which denotes the weight of the electron wave function at the site of the nuclear spin  $\vec{J}_i$ . This interaction of the nuclei on the electron can be seen as an effective Overhauser field

$$g\mu_B \mathbf{B}_{nuc,d} = \sum_i A_i \mathbf{J}_i. \quad (4.5)$$



The total magnetic fields experienced by the electrons in each dot is thus composed of the external field  $\vec{B}_{ext}$  and the Overhauser fields  $\mathbf{B}_{nuc,d}$  in each dot. For the singlet triplet qubit, the difference of the magnetic fields along the quantization axis of the electron spin (chosen to be along the  $z$ -axis)  $\Delta B^z = B_{nuc,L}^z - B_{nuc,R}^z$  experienced by the electrons in the two dots leads to a Zeeman splitting between the  $|\uparrow\downarrow\rangle$  and  $|\downarrow\uparrow\rangle$  configuration. Note that the external field does not influence this splitting as it is homogeneous for both dots. The energy splitting  $\Delta B^z$  leads to rotations about the  $z$ -axis in the Bloch sphere picture (see Fig. 2.1) corresponding to oscillations between the two logical states  $|S\rangle$  and  $|T_0\rangle$  (both in the equatorial plane). Fluctuations of this field have been identified as the dominant source of dephasing.

Plugging these fluctuations into the parameter  $\beta(t)$  in Eq. 4.3 implies three assumptions that are made to describe the noise bath.

- The Overhauser field fluctuations  $\Delta B^z(t)$  can be modeled as a classical Gaussian noise variable  $\Delta B^z(t)$  with  $\langle \Delta B^z \rangle = 0$  and variance  $\sqrt{\langle (\Delta B^z)^2 \rangle}$  typically on the order of a few millitesla [12, 49]. This assumption is motivated by the large number of nuclear spins coupled to the electron and closely relates to the central limit theorem.
- Electron-nuclear spin flip-flop processes  $S^+ J_i^- + S^- J_i^+$ , also present in Eq. 4.3 where  $S^\pm$  ( $J_i^\pm$ ) are the ladder operators for the electron (nuclear) spins, are negligible. This assumption can be assured by applying a sufficiently large magnetic field which suppresses these processes due to energy conservation.
- The model also neglects back action from the qubit state on the noise bath, e.g. hyperfine-induced nuclear spin dynamics such as electron spin-mediated nuclear flip-flop processes of the form  $S^z J_i^+ J_j^-$ . In fact, in e.g. self-assembled InGaAs quantum dots, backaction from the qubit on its environment is the dominant process leading to a decay of the bath state [51]. However, the hyperfine coupling in the lateral dots considered here is much weaker because of a larger spread of the electron wave function compared to the self-assembled dots.

While in principle the nuclei constitute a quantum-mechanical system that has to be simulated accordingly, it is under the assumptions above sufficient to treat the Overhauser field fluctuations as classical spin diffusion characterized by their noise power spectral density. Measurements of the singlet triplet return probability suggest a spectrum of the form

$$S_{\Delta B^z}(\omega) = \frac{S_0}{\omega^2} \quad (4.6)$$

where the constant  $S_0$  determines the overall noise level [47]. Due to the limited nuclear spin-spin interaction strength, a correlation time  $\tau_C = 2\pi/\omega_C$  below which the spin diffusion processes are suppressed, is assumed. This corresponds to a high frequency cutoff

$\omega_C$  above which  $S_{\Delta B_z}(\omega)$  decreases stronger than  $\omega^{-2}$ . Comparison with qubit coherence in free induction decay experiments indicates  $\omega_C/2\pi \approx 10\text{-}100$  kHz [47]. This cutoff has so

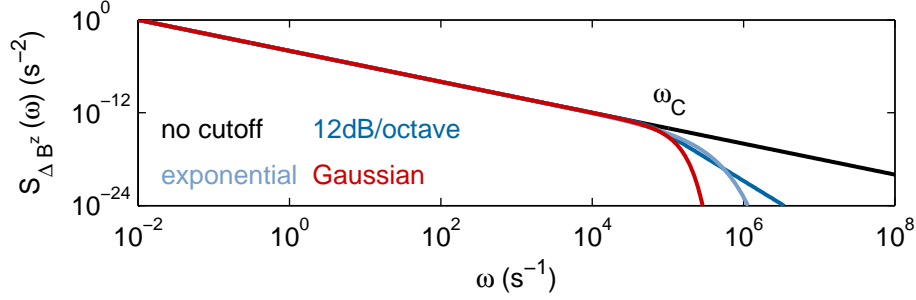


**Figure 4.2:** Spectrum of the Overhauser field fluctuations  $S_{\Delta B_z}(\omega)$  with different cutoff behaviors at  $\omega_C = 2\pi \times 10$  kHz. The black curve is the spectrum defined in Eq. 4.6 with  $S_0 = 10^{-4} \text{ s}^{-2}$ . The dark blue, light blue and red lines correspond to the presence of a 12 dB/octave (equal to  $\omega^{-4}$ ), exponential ( $e^{-\omega/\omega_C}$ ) and Gaussian ( $e^{-(\omega/\omega_C)^2}$ ) cutoff, respectively.

far not been observed experimentally and also its exact form is purely speculative due to a lack of techniques to experimentally access these frequency regions. It is yet desirable to investigate this frequency range to e.g. improve pulse sequence performance through an optimized adaption to the high-frequency behavior and thus extend qubit coherence times. Simple examples for the cutoff could be a stronger polynomial, exponential or Gaussian behavior as illustrated in Fig. 4.2.

Hence, the central question determining the performance and usefulness of my noise spectroscopy scheme applied to the singlet triplet qubits is thus whether it aids the investigation of the cutoff behavior.

#### 4.2.2 1/f noise

In the context of superconducting circuits,  $1/f^\alpha$ -noise has been found to be the dominant source of dephasing in superconducting quantum interference devices [52], charge [53], flux [31, 33, 45, 54] and phase [42, 43] qubits. The origin of this noise may be attributed to critical current fluctuations or charge noise stemming from e.g. charge traps located in the oxides of the Josephson junction. However, the exact microscopic origin remains elusive. Remarkably, the noise spectrum follows a distribution of the form

$$S(\omega) = \frac{S_0}{\omega^\alpha} \quad (4.7)$$

despite of the different realizations for superconducting qubits.  $S_0$  is a constant determining the overall noise amplitude and  $\alpha$  characterizes the frequency-dependence, possibly revealing information about the underlying physical processes. Comparing e.g. Ref. [42]

and Ref. [31] reveals that  $1/f^\alpha$  noise has been found both for very low (up to 0.1 Hz) and very high (above 100 kHz) frequencies. It is yet unclear whether the same noise spectrum also applies to the frequencies within the gap of these measurements. Investigating this region would thus shed light onto the question whether the  $1/f$  spectra extend over the whole frequency range and might be contributed to a single physical process.

It should be noted that  $1/f$ -like noise spectra have been shown to be very universal in the context of electronics and solid-state physics [55, 56]. Hence, this noise can be regarded to be very generic.



## Measurement scheme

The measurement scheme is illustrated in Fig. 5.1. It consists of initializing a  $\hat{\sigma}_x$  eigenstate followed by a free evolution of the qubit under the influence of the noise bath, represented by the dephasing Hamiltonian in Eq. 4.1, for time  $\tau_{1,2}$ . The qubit state is then read out by performing a projective single-shot measurement. After a delay time  $\Delta t$  the cycle is repeated. The autocorrelation function of the two single-shot readouts in dependence of

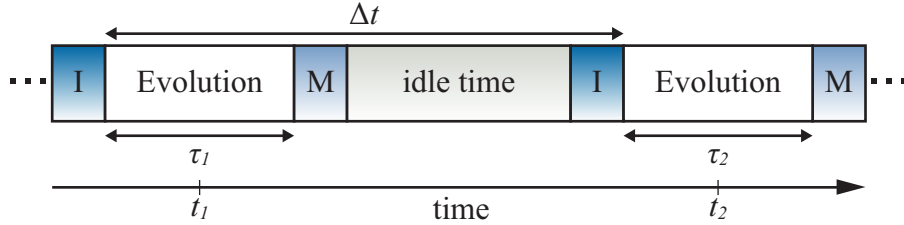


**Figure 5.1:** Illustration of the measurement scheme consisting of two successive initialization (I), evolution and measurement (M) cycles separated by an idle time determined by the delay time  $\Delta t$ . The duration of the two evolutions is defined by  $\tau_{1,2}$ .

the delay time can then be calculated by sweeping  $\Delta t$ . Note that this technique allows to access the regime of large errors with  $\tau \gtrsim T_2^*$  compared to the small-error limit  $\tau \ll T_2^*$  used in previous approaches. The durations of initializing and measuring the qubit set a lower bound on the delay times accessible with this technique. For the singlet triplet qubit, initialization and single-shot measurement have been shown to be on the order of 30 ns and 100 ns, respectively, which is fast compared to typical evolution times in e.g. spin echo experiments [15]. For superconducting qubits, however, initialization is often realized through relaxation and thus on the order of  $T_1$ , which is assumed to be large compared to the duration of the measurement cycle. This constraint can be circumvented by replacing the long initialization with a projective measurement [23] which is fast in superconducting qubits and also reveals the information necessary to calculate the autocorrelation function. The ability to use delay times on the order of the evolution times is a crucial advantage of this technique compared to direct measurement-based noise spectroscopy. For the latter, the highest frequencies accessible are limited by the averaging

necessary to measure the qubit state as described above [29, 42]. Thus, correlating single-shot measurements drastically increases the frequency range and allows to access the noise spectrum between direct and pulse sequence-based spectroscopy.

If the preparation and readout axis of the respective qubit system does not coincide with the axis spanned by the superposition states, at most two  $\frac{\pi}{2}$ -pulses per evolution time are required to initialize and measure the state. For e.g. the singlet triplet qubit, however, no such pulses are needed as initialization and measurement are performed directly on the singlet state. Imperfect pulse control limiting the usage of pulse sequences with a large number of  $\pi$ -pulses will thus have a negligible or no effect at all on the presented measurement scheme. [45]

## Correlation function

In this chapter, I will present the mathematical derivation of the autocorrelation function used for the measurement scheme described in the previous part.

The evolution of a superposition state  $|\pm\rangle$  during an evolution time  $t$  under the influence of an unitary operator  $U(t) = \exp\left(-i\frac{\hat{H}}{\hbar}t\right)$  composed of the dephasing Hamiltonian introduced in Eq. 4.1 can be described as a phase picked up by the two basis states  $|0\rangle$  and  $|1\rangle$

$$\begin{aligned} |\psi(t)\rangle &= \frac{1}{\sqrt{2}} \left( e^{-i\Delta\phi(t)/2} |0\rangle \pm e^{i\Delta\phi(t)/2} |1\rangle \right) \\ &= \frac{e^{-i\Delta\phi(t)/2}}{\sqrt{2}} \left( |0\rangle \pm e^{i\Delta\phi(t)} |1\rangle \right) \end{aligned} \quad (6.1)$$

where the phase

$$\Delta\phi(t) = \int_0^t \beta(t') dt' \quad (6.2)$$

is determined by the integration of the noise variable  $\beta(t)$  over the evolution time. Note that the constant energy splitting  $\Omega$  has been set to zero. The effects of the more general case with a finite  $\Omega$  will be considered below. The probability  $P$  to measure the initialized state  $|\psi(0)\rangle = |\pm\rangle$  after an evolution of duration  $t$  is given by the projection of this state onto the qubit state  $|\psi(t)\rangle$

$$P(t) = |\langle \pm | \psi(t) \rangle|^2 = \cos^2 \left( \frac{\Delta\phi(t)}{2} \right) = \frac{1}{2} + \frac{1}{2} \cos(\Delta\phi(t)). \quad (6.3)$$

To simplify the expression for the autocorrelation function below by suppressing uninteresting free induction decay terms, I will drop the constants in this chapter and define the return probability as  $P(t) = \cos(\Delta\phi(t))$  which trivially maps the measurement result  $P \in [0, 1]$  onto  $P \in [-1, 1]$ . The two-point autocorrelation function is then given by

$$\langle P(t_1)P(t_2) \rangle = \frac{1}{2} [\langle \cos(\Delta\phi(t_1) + \Delta\phi(t_2)) \rangle + \langle \cos(\Delta\phi(t_1) - \Delta\phi(t_2)) \rangle] \quad (6.4)$$

where  $\langle \dots \rangle$  denotes averaging over the initial configurations of the noise bath  $\beta(t)$ . Using Euler's formula  $\cos(x) = \frac{1}{2}(e^{ix} + e^{-ix})$  leads to expressions of the form  $\langle e^{\pm i(\Delta\phi(t_1) \pm \Delta\phi(t_2))} \rangle$ . For Gaussian variables with zero mean the only nonzero cumulant is the variance so that  $\langle e^{ix} \rangle = \exp\left(\sum_{k=1}^{\infty} \frac{i^k}{k!} \kappa_k\right) = e^{-\frac{1}{2}\langle x^2 \rangle}$  where  $\kappa_k$  are the cumulants of  $x$  [57]. As  $\beta(t)$  defined in Eq. 2.3 obeys a Gaussian distribution with  $\langle \beta(t) \rangle = 0$ , also  $\Delta\phi(t_1) \pm \Delta\phi(t_2)$  fulfills this requirement because the sum of two Gaussian variables remains Gaussian. Hence, the autocorrelation function can be simplified to

$$\begin{aligned} \langle P(t_1)P(t_2) \rangle &= \frac{1}{2}e^{-\frac{1}{2}\langle (\Delta\phi(t_1) + \Delta\phi(t_2))^2 \rangle} + \frac{1}{2}e^{-\frac{1}{2}\langle (\Delta\phi(t_1) - \Delta\phi(t_2))^2 \rangle} \\ &= \frac{1}{2}e^{-\frac{1}{2}\chi_+(t_1, t_2)} + \frac{1}{2}e^{-\frac{1}{2}\chi_-(t_1, t_2)}. \end{aligned} \quad (6.5)$$

The expressions  $\chi_{\pm}$  consist of integrals over the noise autocorrelation function of the form  $\int \int dt' dt'' \langle \beta(t')\beta(t'') \rangle$  similar to those for qubit coherence under the application of pulse sequences. Ref. [40] introduced a notation to express these terms via the noise spectral density  $S_{\beta}(\omega)$  and a filter function  $F(\omega t)$  containing informations about the sequence

$$\int_0^t \int_0^t dt' dt'' \langle \beta(t')\beta(t'') \rangle c(t', t'') = \int_0^{\infty} \frac{d\omega}{\pi} S_{\beta}(\omega) \frac{F(\omega t)}{\omega^2}. \quad (6.6)$$

The factor  $c(t', t'')$  conveys the details of the pulse sequence and switches between  $\pm 1$  whenever a  $\pi$ -pulse is applied. As our measurement scheme does not include any such pulses,  $c(t', t'') = 1 \forall t', t''$ . The filter function  $F(\omega t)$  is characteristic for every pulse sequence and includes information about how many and when  $\pi$ -pulses are applied. Moreover, it determines where the sequence is sensitive. For e.g. the spin echo,  $F(\omega t) \sim (\omega t)^4$  for  $\omega t \ll 4$  and thus effectively suppresses low-frequency noise.

The terms  $\chi_{\pm}$  can be expressed according to Eq. 6.6 via their spectrum as defined in Eq. 4.2

$$\begin{aligned} \chi_{\pm}(t_1, t_2) &= \left\langle \left( \int_{t_1-\tau_1/2}^{t_1+\tau_1/2} \beta(t') dt' \pm \int_{t_2-\tau_2/2}^{t_2+\tau_2/2} \beta(t') dt' \right)^2 \right\rangle \\ &= \int_{t_1-\tau_1/2}^{t_1+\tau_1/2} \int_{t_1-\tau_1/2}^{t_1+\tau_1/2} \langle \beta(t')\beta(t'') \rangle dt' dt'' + \int_{t_2-\tau_2/2}^{t_2+\tau_2/2} \int_{t_2-\tau_2/2}^{t_2+\tau_2/2} \langle \beta(t')\beta(t'') \rangle dt' dt'' \\ &\quad \pm \int_{t_1-\tau_1/2}^{t_1+\tau_1/2} \int_{t_2-\tau_2/2}^{t_2+\tau_2/2} \langle \beta(t')\beta(t'') \rangle dt' dt'' \\ &= \int_0^{\infty} \frac{d\omega}{\pi} S_{\beta}(\omega) \frac{F_{\pm}(\omega, \tau_1, \tau_2, \Delta t)}{\omega^2} \end{aligned} \quad (6.7)$$



where in the last step  $t_1, t_2$  have been expressed as  $\Delta t = t_2 - t_1$  because for an unpolarized noise bath only the relative position of the two measurements is of physical relevance. Consequently,  $\chi_{\pm}(t_1, t_2)$  can be rewritten as  $\chi_{\pm}(\tau_1, \tau_2, \Delta t)$ . The filter function of the measurement scheme is determined by integrals  $\frac{\omega^2}{2} \int \int dt' dt'' e^{i\omega(t' - t'')}$  where the integration limits are given by the parameters  $\tau_1, \tau_2$  and  $\Delta t$ . Calculating these integrals leads to

$$F_{\pm}(\omega, \tau_1, \tau_2, \Delta t) = 4 \sin^2 \left( \frac{\omega \tau_1}{2} \right) + 4 \sin^2 \left( \frac{\omega \tau_2}{2} \right) \pm 8 \cos(\omega \Delta t) \sin \left( \frac{\omega \tau_1}{2} \right) \sin \left( \frac{\omega \tau_2}{2} \right). \quad (6.8)$$

Note that the first two terms are identical to filter functions for free induction decay experiments of duration  $\tau_{1,2}$  while the last term arises due to the correlation between them [40].

To further simplify the autocorrelation function I assume  $\tau_1 = \tau_2 = \tau$  for the moment and discuss effects of asymmetric measurement schemes below. Plugging the filter functions into Eq. 6.7 leads to

$$\begin{aligned} \chi_+(\tau, \Delta t) &= 16 \int_0^\infty \frac{d\omega}{\pi} S_\beta(\omega) \frac{\sin^2 \left( \frac{\omega \tau}{2} \right)}{\omega^2} \cos^2 \left( \frac{\omega \Delta t}{2} \right) \\ \chi_-(\tau, \Delta t) &= 16 \int_0^\infty \frac{d\omega}{\pi} S_\beta(\omega) \frac{\sin^2 \left( \frac{\omega \tau}{2} \right)}{\omega^2} \sin^2 \left( \frac{\omega \Delta t}{2} \right). \end{aligned} \quad (6.9)$$

The filter functions of these two terms are shown in Fig. 6.1 (a). It is apparent both from the figure and from Eq. 6.9 that  $F_+$  is concentrated at  $\omega = 0$  corresponding to a high sensitivity to low-frequency noise. As this noise is dominant for most spectra such as the  $1/f$  spectrum and the Overhauser field fluctuation spectrum introduced before,  $\chi_+(\tau, \Delta t)$  will be large and thus its contribution to the autocorrelation function in Eq. 6.5 is negligible. The close analogy of  $\chi_+(\tau, \Delta t)$  with a free induction decay is obvious for  $\Delta t \rightarrow 0$  as in this case the filter functions are identical:  $F_+(\omega, \tau, 0) = F_{FID}(\omega \tau) = 4 \sin^2 \left( \frac{\omega \tau}{2} \right)$ .  $\chi_+$  thus decays on a time scale much smaller than  $T_2^*$ .

$F_-$  is characterized by a peak that depends on the parameters  $\tau$  and  $\Delta t$ . Its sensitivity to strong low-frequency noise is negligible so that  $\chi_-(\tau, \Delta t)$  can be on the order of one and thus its exponential is measurable. For  $\Delta t = \tau$ ,  $F_-$  is identical to the filter function of a spin echo experiment (compare Fig. 6.1 (a) and (c)). In fact,  $F_-$  can be regarded as its two-parameter generalization. Varying  $\tau$  and  $\Delta t$  shifts the height and position of the peak in the frequency domain as shown in Fig. 6.1 (a). This is the crucial advantage of the presented measurement scheme: suitable choice of the evolution and delay time allows to tailor the sensitivity of the autocorrelation measurement as needed. Consider short evolution times compared to the delay time and the frequency regions of interest. In this case, the dominant exponent of the autocorrelation function becomes

$$\chi_-(\tau, \Delta t) = 4\tau^2 \int_0^\infty \frac{d\omega}{\pi} S_\beta(\omega) \sin^2 \left( \frac{\omega \Delta t}{2} \right). \quad (6.10)$$

The evolution time acts as a gain factor determining the overall magnitude of  $\chi_-$  while the delay time sets the frequency range that it is sensitive to. By sweeping  $\Delta t$ , the sensitivity of the autocorrelation measurement is swept in the frequency domain giving access to the whole noise spectrum.

Considering small noise variations  $\tau^2 (\langle \beta(t)\beta(t + \Delta t) \rangle - \langle \beta^2 \rangle) \ll 1$  reveals an even more direct approach to measure the noise spectrum. In this regime, the exponent  $\chi_-(\tau, \Delta t)$  is small. Approximating the autocorrelation function in Eq. 6.5 then leads to

$$\langle P(t)P(t + \Delta t) \rangle \approx \frac{1}{2} + \frac{\tau^2}{2} \langle \beta(t)\beta(t + \Delta t) \rangle - \frac{\tau^2}{2} \langle \beta^2 \rangle \quad (6.11)$$

which allows to direct measurement of the noise spectrum via correlating the single-shot readouts. The effect of asymmetric pulses with  $\tau_1 \neq \tau_2$  is shown in Fig. 6.1 (b) and leads to a reduction of the peak height and an increased sensitivity of  $F_-(\omega, \tau_1, \tau_2, \Delta t)$  to low-frequency noise. This introduction of FID-type effects is not beneficial and would hamper the ability to decouple the sequence from low-frequency noise while choosing the frequency it is sensitive to. Thus, asymmetric pulse lengths are not experimentally relevant and will not be discussed further.

For a finite energy splitting, the phase in Eq. 6.2 becomes  $\Delta\phi(t) = \Omega t + \int_0^t \beta(t') dt'$ . This leads to an autocorrelation function given by

$$\langle P(t)P(t + \Delta t) \rangle = \frac{1}{2} \cos[\Omega(\tau_1 + \tau_2)] e^{-\frac{1}{2}\chi_+(\tau_1, \tau_2, \Delta t)} + \frac{1}{2} \cos[\Omega(\tau_1 - \tau_2)] e^{-\frac{1}{2}\chi_-(\tau_1, \tau_2, \Delta t)}. \quad (6.12)$$

Thus, for the experimentally relevant case of symmetric measurement sequences, a finite energy splitting does not affect the previous results as it only adds oscillations to the negligible term.

Comparing Fig. 6.1 (a) and (c) shows that using the autocorrelation function is an excellent technique to investigate the noise spectrum and bridge the gap that remains between the sensitivity of free induction decay and pulse sequence experiments.

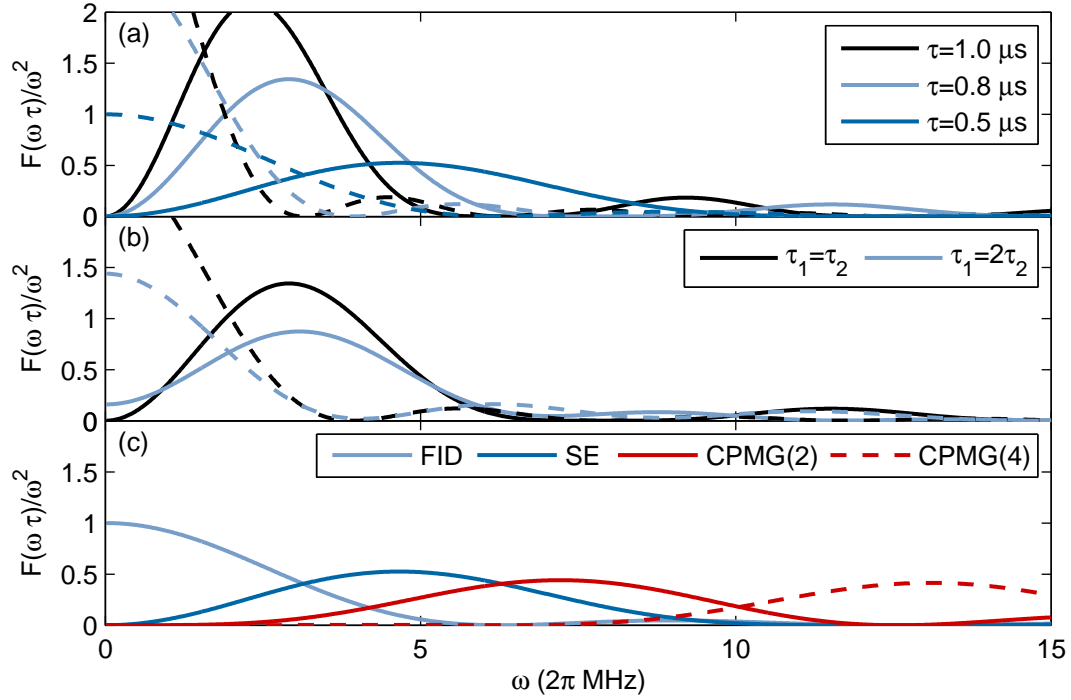


**Figure 6.1:** Filter function of the autocorrelation function.

- (a) Filter function of  $\chi_{\pm}$  for different evolution times  $\tau_1 = \tau_2 = \tau$ . The solid (dashed) line corresponds to  $F_{-}(\omega, \tau, \Delta t)/\omega^2$  ( $F_{+}(\omega, \tau, \Delta t)/\omega^2$ ).  $\Delta t = \tau$  for each curve. Suitable choice of the parameters  $\Delta t$  and  $\tau$  allows to both shift the peak in the frequency domain and control its magnitude. This corresponds to tailoring the sensitivity of  $F_{-}$  to the frequency regions of interest. It is apparent that the filter function of  $\chi_{+}$  has a high weight at low frequencies while the maximum sensitivity of  $\chi_{-}$  can be shifted. Note that the dark blue dashed and solid line are identical to the free induction decay and spin echo filter functions in (c). For details see text.
- (b) Filter function of  $\chi_{\pm}$  for asymmetric measurement schemes with  $\tau_1 \neq \tau_2$ . The solid (dashed) line corresponds to  $F_{-}(\omega, \tau_1, \tau_2, \Delta t)/\omega^2$  ( $F_{+}(\omega, \tau_1, \tau_2, \Delta t)/\omega^2$ ).  $\Delta t = \tau_1 = 0.8 \mu\text{s}$ . Different pulse lengths lead to a reduction of the filter function corresponding to a reduced sensitivity.
- (c) Filter function for different pulse sequences. The evolution times for each curve is  $\tau = 1 \mu\text{s}$ . The decoupling mechanism from low-frequency contributions of the noise spectrum is apparent when comparing the pulse sequence filter functions to that of the FID experiment. For e.g. the spin echo, contributions with frequencies  $\omega \ll \frac{4}{\tau} = 4 \times 10^6 \text{ s}^{-1}$  are effectively suppressed because the filter function is insensitive in this region. Pulse sequences employing more  $\pi$ -pulses effectively shift the sensitive region to higher frequencies as indicated by the number in brackets corresponding to the number of pulses applied.



## Simulations

In this chapter, simulations illustrating the usefulness of the presented measurement technique to investigate noise spectra will be presented.

### 7.1 Lorentzian

To start with a simple and analytically treatable case, the measurement scheme will be applied to a Lorentzian noise spectrum. These spectra can be considered to be very generic for both the singlet triplet and also superconducting qubits in the sense that they describe nuclear spin diffusion processes up to the assumed high-frequency cutoff and may also lead to the  $1/f^\alpha$  noise spectrum if a superposition of many Lorentzians is assumed. I will therefore first consider the effect of a single Lorentzian spectrum and then add a second to illustrate how a superposition can be identified.

#### 7.1.1 One Lorentzian

The spectrum of a Lorentzian

$$S(\omega) = \frac{S_0}{1 + \left(\frac{\omega}{\omega_C}\right)^2} \quad (7.1)$$

is characterized by its overall noise magnitude  $S_0$  and the cutoff frequency  $\omega_C$  below which the noise is white. For this spectrum, the autocorrelation function can be calculated analytically leading to

$$\chi_{\pm}(\tau, \Delta t) = 2 \frac{S_0}{\omega_C} \left[ \omega_C \tau - 1 + e^{-\omega_C \tau} \mp e^{-\omega_C \Delta t} \pm e^{-\omega_C \Delta t} \cosh(\omega_C \tau) \right]. \quad (7.2)$$

For small evolution times, such that  $\omega_C \tau \ll 1$ , this expression simplifies to

$$\begin{aligned} \chi_+(\tau, \Delta t) &= 2S_0\omega_C\tau^2 \cosh\left(\frac{\omega_C\Delta t}{2}\right) e^{-\frac{\omega_C\Delta t}{2}} \\ \chi_-(\tau, \Delta t) &= 2S_0\omega_C\tau^2 \sinh\left(\frac{\omega_C\Delta t}{2}\right) e^{-\frac{\omega_C\Delta t}{2}}. \end{aligned} \quad (7.3)$$

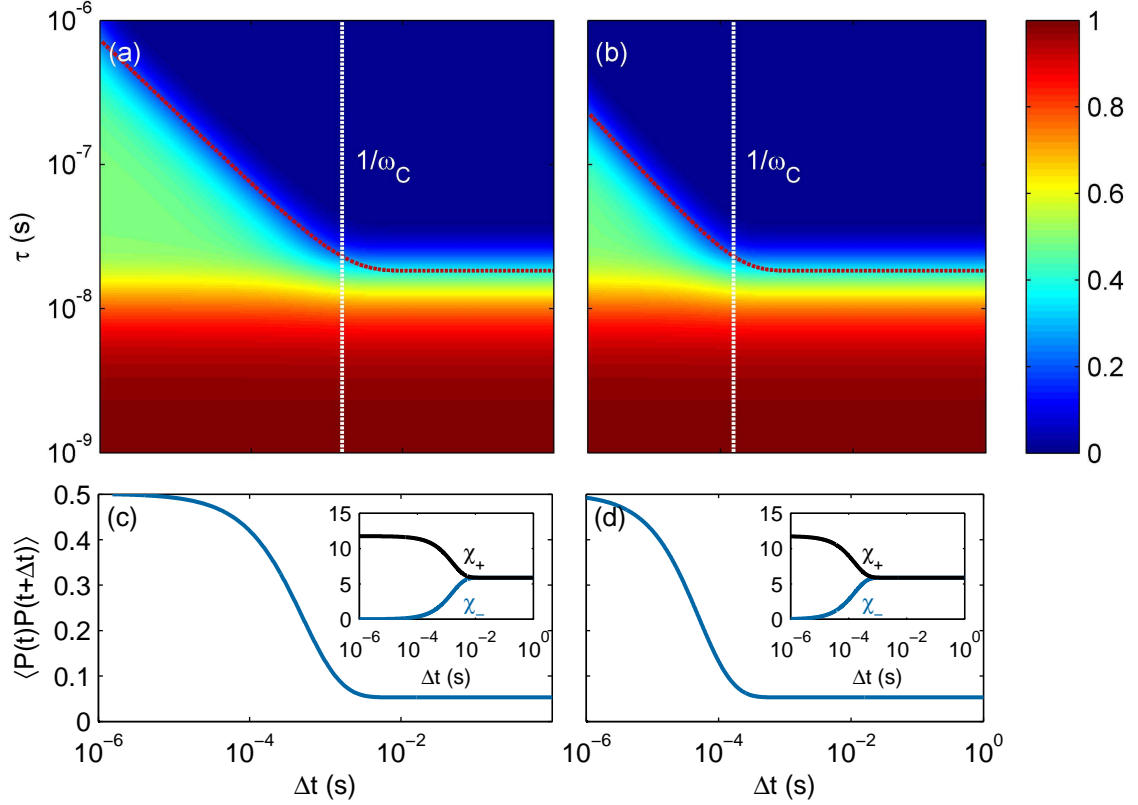


**Figure 7.1:** (a) Autocorrelation function shown as colorscale for a Lorentzian noise spectrum with  $\omega_C = 2\pi \times 100$  Hz and  $S_0 = \frac{2}{\pi\omega_C} \left(\frac{g\mu_B}{\hbar}\right)^2 \times (2.5 \text{ mT})^2$ . The colorscale is given on the right. The  $x$ -axis is identical to (c). The kink at  $\Delta t \sim \frac{1}{\omega_C}$  clearly indicates the transition of white noise to the  $\omega^{-2}$  behavior. The red dotted line illustrates where  $\chi_-(\tau, \Delta t) = 2$ . (b) Same as (a) for  $\omega_C = 2\pi \times 1$  kHz. (c), (d) Linecuts through (a) and (b), respectively, at  $\tau = 31$  ns. Insets: corresponding exponents  $\chi_{\pm}(31 \text{ ns}, \Delta t)$ .

In this regime, the effect of the evolution time  $\tau$  acting as a control knob to set the overall magnitude of  $\chi_{\pm}$  is obvious. Fig. 7.1 (a) and (b) show the autocorrelation as a function of the evolution and delay time for  $\omega_C = 2\pi \times 100$  Hz and  $\omega_C = 2\pi \times 1$  kHz, respectively. The normalization constant  $S_0$  is defined by  $\int_0^\infty d\omega S(\omega) = \left(\frac{g\mu_B}{\hbar}\right)^2 \times (2.5 \text{ mT})^2$  which relates to the nuclear Overhauser field fluctuations. The kink at  $\Delta t \sim \omega_C^{-1}$  shows the characteristic effect of the cutoff frequency and marks the transition from probing the low-frequency white noise to the  $\omega^{-2}$  regime with the measurement sequence. For evolution times where the transition is clearly pronounced, the maximum autocorrelation of  $\frac{1}{2}$  (light green) indicates that  $e^{-\frac{1}{2}\chi_+(\tau, \Delta t)}$  is negligible as discussed before. This can also be seen in the insets of Fig. 7.1 (c) and (d) where  $\chi_+$  is large whereas  $\chi_-$  is small enough for its exponential to be measurable for small delay times. Experimentally,  $\tau$  can be chosen such that the decay appears on a measurable time scale and thus allows for identification of the cutoff frequency. The red dotted line indicates the position of the

decay of correlation defined as  $\frac{1}{2}e^{-\frac{1}{2}\chi_-(\tau, \Delta t)} = \frac{1}{2}e^{-1}$ . It can be derived from Eq. 7.3 that this condition is fulfilled for

$$\tau = \sqrt{\frac{2}{S_0\omega_C(1 - e^{-\omega_C\Delta t})}}. \quad (7.4)$$

The slight deviation from the contour of the autocorrelation function at  $\Delta t \gtrsim \frac{1}{\omega_C}$  indicates non-negligible contributions of  $\chi_+(\tau, \Delta t)$  as  $\chi_+$  and  $\chi_-$  are equally large in this region (see inset in Fig. 7.1 (c) and (d)).

The simulations show, that the delay time for which the autocorrelation decreases is closely related to the cutoff frequency and may be controlled with the evolution time. Thus, measuring the autocorrelation function indeed reveals  $\omega_C$ . Note that the plateau at  $\Delta t \gtrsim \frac{1}{\omega_C}$  can moreover be used to determine the overall noise magnitude  $S_0$  as this region corresponds to the white noise part of the spectrum.

### 7.1.2 Two Lorentzians

The spectrum of  $1/f^\alpha$  noise may originate from a superposition of Lorentzian spectra with different cutoff frequencies. To investigate whether the measurement scheme allows to detect this superposition I consider a spectrum composed of two Lorentzians:

$$S(\omega) = \sum_{i=1}^2 \frac{S_{0,i}}{1 + \left(\frac{\omega}{\omega_i}\right)^2}. \quad (7.5)$$

The normalization constants are again chosen to result in a nuclear Overhauser field of 2.5 mT such that  $S_{0,i} = \frac{1}{2} \frac{2}{\pi\omega_i} \left(\frac{g\mu_B}{\hbar}\right)^2 \times (2.5 \text{ mT})^2$ .  $\chi_\pm(\tau, \Delta t)$  can be calculated as a superposition of Eq. 7.2 with two different cutoff frequencies. Fig. 7.2 shows the autocorrelation function for this spectrum, which reveals two distinctive features characteristic for the presence of the respective cutoff frequency. This effect is also visible in Fig. 7.2 (c) and (d) which depict the autocorrelation function for the two different spectra at  $\tau = 31 \text{ ns}$ .

Qualitatively, the presence of each Lorentzian causes a kink in the autocorrelation function at  $\Delta t \sim \frac{1}{\omega_C}$ . The identification and distinction of different cutoff frequencies will be limited experimentally by the signal-to-noise ratio. For the simulations shown here, the difference in height of the two plateaus at  $\Delta t \gtrsim \frac{1}{\omega_i}$  corresponds to 14 % of the maximum autocorrelation of  $\frac{1}{2}$ . To distinguish the two Lorentzians, the noise must thus not account for more than e.g. 10 % of the maximum signal, which can be ensured by averaging over a sufficient number of single-shot measurements.

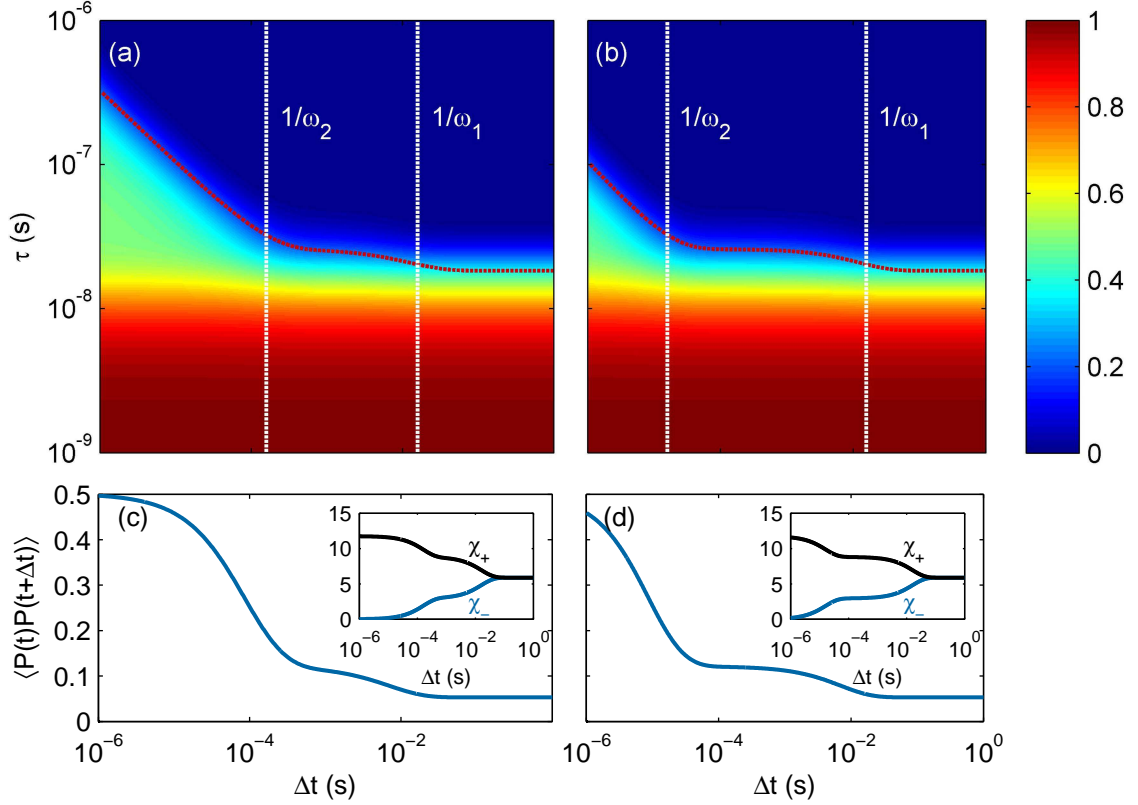


**Figure 7.2:** (a) Autocorrelation function shown as colorscale for a spectrum consisting of two Lorentzians with  $\omega_1 = 2\pi \times 10$  Hz and  $\omega_2 = 2\pi \times 1$  kHz. The  $x$ -axis is identical to (c). Two kinks at  $\Delta t \sim \frac{1}{\omega_1}$  and  $\Delta t \sim \frac{1}{\omega_2}$  with a plateau in between appear, corresponding to the two cutoff frequencies. The red dotted line is defined as before. (b) Same as (a) for  $\omega_1 = 2\pi \times 10$  Hz and  $\omega_2 = 2\pi \times 10$  kHz. (c), (d) Linecuts through (a) and (b), respectively, at  $\tau = 31$  ns. Insets: corresponding exponents  $\chi_{\pm}(31 \text{ ns}, \Delta t)$ .

## 7.2 Nuclear spin bath

After illustrating the effect of the measurement scheme and how it may be used to extract properties of the underlying noise spectrum with the two simple examples above, I will now consider a realistic spectrum which mimics the Overhauser field fluctuations in the singlet triplet qubit [47]. Specifically, a spectrum of the form

$$S_{\Delta B_z}(\omega) = \frac{S_0}{1 + \left(\frac{\omega}{\omega_L}\right)^2} \times e^{-\left(\frac{\omega}{\omega_E}\right)^\gamma} \quad (7.6)$$

will be assumed where the lower cutoff  $\omega_L$  ensures numerical convergence. Consistent with experiments, this cutoff is set to  $\omega_L = 2\pi \times 0.1$  Hz corresponding to an oscillation with a period of 10 s which is static to  $\sim 10^{-5}$  for even the longest dynamical decoupling experiments with  $T_2 \approx 200 \mu\text{s}$  involving 16  $\pi$ -pulses [13]. I chose  $S_0$  such that



$\int_0^\infty d\omega S_{\Delta B_z}(\omega) = (\frac{q\mu_B}{\hbar})^2 \langle \Delta B_z^2 \rangle$  where  $\sqrt{\langle \Delta B_z^2 \rangle} = 2.5 \text{ mT}$  is consistent with experiments [12]. To investigate the cutoff behavior, it is both interesting at which frequencies and how strongly the nuclear spin diffusions are suppressed, corresponding to the parameters  $\omega_E$  and  $\gamma$ , respectively.

The autocorrelation function can be calculated numerically by plugging the spectrum given in Eq. 7.6 into Eq. 6.9. Fig. 7.3 (a) shows this function for an exponential cutoff at 10 kHz with different evolution times. The maximum autocorrelation of  $\frac{1}{2}$  indicates the limit

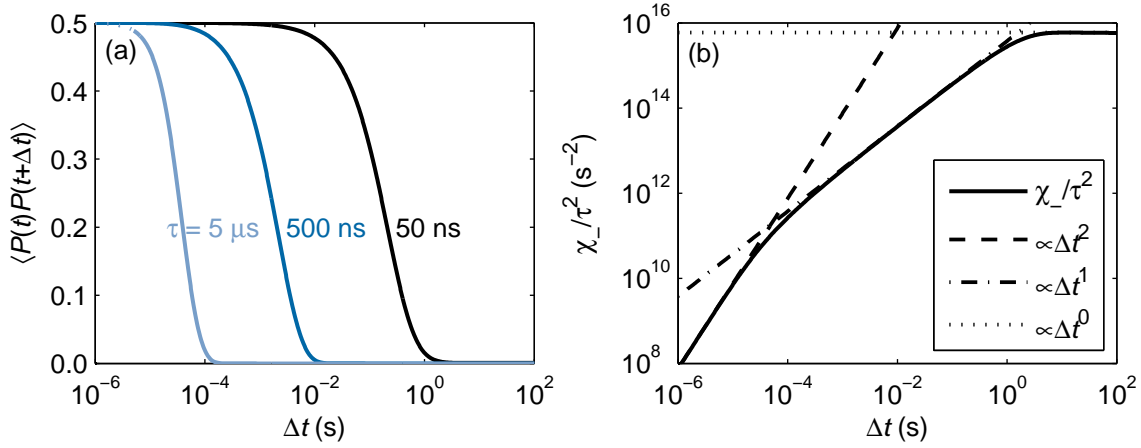


**Figure 7.3:** (a) Autocorrelation for the nuclear spin diffusion with exponential cutoff at 10 kHz for evolution time 5  $\mu\text{s}$ , 500 ns and 50 ns, respectively. The dotted region of the light blue curve indicates that the autocorrelation function does not exist there as  $\Delta t < \tau$ . (b) Dominant exponent of the autocorrelation function. The renormalization by  $\tau^2$  removes the dependence on the evolution time. Three different regimes associated to the Lorentzian and exponential cutoff frequency are visible leading to quadratic, linear and constant behavior. The dashed, dash-dotted and dotted line are the approximations defined in Eq. 7.7.

of small evolution times where  $e^{-\frac{1}{2}\chi_+(\tau, \Delta t)}$  is negligible. The effect of  $\tau$  controlling the magnitude of  $\chi_{\pm}(\tau, \Delta t)$  is apparent by the shift of the decay for different evolution times. Fig. 7.3 (b) shows the exponent  $\frac{\chi_-}{\tau^2}$  where the renormalization removes the dependence on the evolution time. Three different regimes for delay times corresponding to frequencies above  $\omega_E$ , between  $\omega_L$  and  $\omega_E$  and below  $\omega_L$  are visible. They can be approximated by

$$\chi_-(\tau, \Delta t) \approx \begin{cases} \frac{a}{\pi} c^2 \omega_E \omega_L^2 \tau^2 S_0 \Delta t^2 & \Delta t \ll \omega_E^{-1} \\ c^2 \omega_L^2 \tau^2 S_0 \Delta t & \omega_E^{-1} \ll \Delta t \ll \omega_L^{-1} \\ 2c^2 \frac{\tau^2}{\pi} (\langle \Delta B_z^2 \rangle)^2 & \Delta t \gg \omega_L^{-1}, \end{cases} \quad (7.7)$$

where  $c = \frac{q\mu_B}{\hbar}$  and  $a = \Gamma\left(\frac{1}{\gamma} + 1\right)$  is given in terms of the Gamma function  $\Gamma(x)$ . For an exponential (Gaussian) cutoff,  $a = 1$  ( $a = \frac{\sqrt{\pi}}{2}$ ). In the second line I made use of the fact that  $\sin^2\left(\frac{\omega \Delta t}{2}\right) / \left(\frac{\omega \Delta t}{2}\right)^2 \rightarrow \frac{2\pi}{\Delta t} \delta(\omega)$  for  $\omega \Delta t \gg 2$ .

Different exponential behaviors, corresponding to different parameters  $\gamma$ , will be observable when the measurement scheme is used to probe the spectrum at the high-frequency cutoff, corresponding to  $\Delta t \sim \omega_E^{-1}$ . This can also be concluded from Eq. 7.7 where different  $\gamma$  manifest themselves in different normalization constants  $S_0$  and the parameter  $a$ . Fig. 7.4 (a) and (b) show  $\chi_-(\tau, \Delta t)$  for an exponential and Gaussian cutoff at  $\tau = 5 \mu\text{s}$  and  $450 \text{ ns}$ , respectively, illustrating the difference of the two cutoffs. For short delay times on the

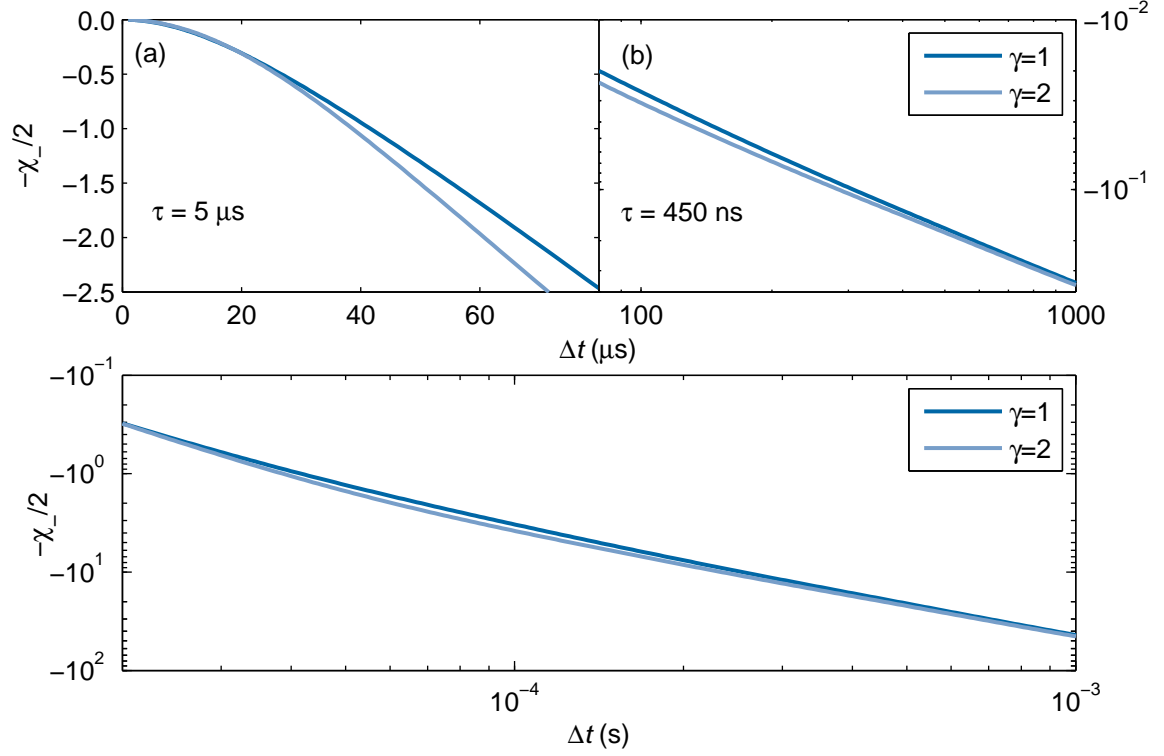


**Figure 7.4:**  $-\chi_-(\tau, \Delta t)/2$  for  $\tau = 5 \mu\text{s}$  with exponential and Gaussian cutoff in dark and light blue, respectively, at  $\omega_E = 10 \text{ kHz}$ . (b) Same as (a) for an evolution time of  $450 \text{ ns}$ . The two curves split due to their different cutoff behavior and merge again at longer delay times when the spectrum below the cutoff is probed. (c)  $\chi_-$  for  $\tau = 5 \mu\text{s}$  showing the whole range of splitting and merging as illustrated in detail in (a) and (b).

order of  $\Delta t \gtrsim \omega_E^{-1} = 16 \mu\text{s}$ , the lines split due to the different cutoff behavior. For longer delay times, when the spectrum below  $\omega_E$  is probed, this splitting vanishes as for  $\Delta t \gtrsim \omega_L^{-1}$  the autocorrelation is only determined by the rms Overhauser field  $\langle \Delta B_z^2 \rangle$  regardless of the cutoff behavior. However, Fig. 7.4 (c) illustrates that the difference of a spectrum with exponential and Gaussian cutoff is small and thus hard to detect compared to the total magnitude of the autocorrelation as  $\chi_-(\tau, \Delta t)$  varies over several orders of magnitude while sweeping the delay time. This relation will hamper the experimental investigation of  $\gamma$ .

To overcome this problem, I will use the evolution time to compensate for a reduction

of  $\chi_-(\tau, \Delta t)$  due to the swept delay time by simultaneously varying the evolution time. Specifically,  $\tau$  is chosen such that the linear part of  $\chi_-(\tau, \Delta t)$  in Eq. 7.7 is constant. This condition can be fulfilled by

$$\tau = \frac{2\hbar}{g\mu_B\omega_L\sqrt{S_0\Delta t}} \quad (7.8)$$

and leads to an autocorrelation of  $\frac{1}{2}e^{-\frac{1}{2}\chi_-(\tau, \Delta t)} = \frac{1}{2}e^{-2}$  for  $\omega_E^{-1} \ll \Delta t \ll \omega_L^{-1}$ . Fig. 7.5 shows that this indeed allows to distinguish the different cutoffs on a measurable scale. The presence of the cutoff can be inferred at  $\Delta t \sim \omega_E^{-1} = 16 \mu\text{s}$  ( $31 \mu\text{s}$ ) for the black (dark blue) curve leading to a characteristic slope compared to the absence of a high-frequency cutoff (light blue curve). In an experiment, one is only able to vary  $\tau \propto \frac{1}{\sqrt{\Delta t}}$  as the parameter  $S_0$  may be unknown. Choosing the evolution time such that the signal is well measurable allows then to determine the overall noise magnitude from the height of the plateau at  $\Delta t \gg \omega_E^{-1}$ . The inset of Fig. 7.5 shows the effect of the simultaneous variation

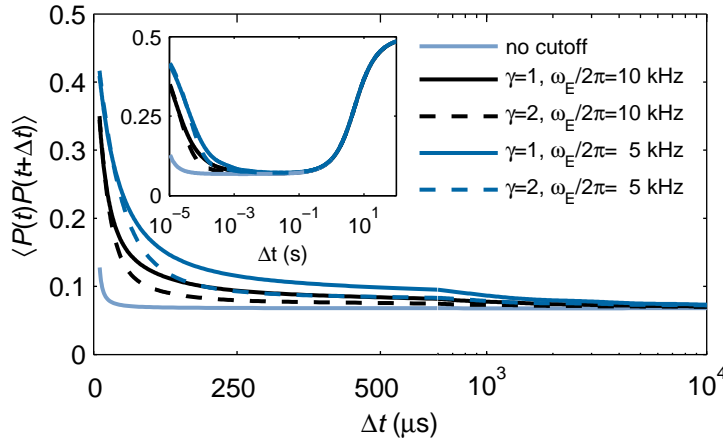


**Figure 7.5:** Autocorrelation for the nuclear spin diffusion spectrum. The light blue curve denotes the absence of a cutoff corresponding to a Lorentzian with  $\frac{\omega_L}{2\pi} = 0.1$  Hz. The solid (dashed) black and dark blue curves represent the autocorrelation function with an exponential (Gaussian) cutoff at  $\frac{\omega_E}{2\pi} = 10$  kHz and 5 kHz, respectively. The evolution time  $\tau \propto \sqrt{\Delta t}^{-1}$  is swept to keep the linear part of  $\chi_-(\tau, \Delta t)$  as described in Eq. 7.7 constant. Note that for  $\Delta t \geq 600 \mu\text{s}$ , the time scale is logarithmic. Inset: Autocorrelation function for delay times up to 10 s. For  $\Delta t \gtrsim \omega_L^{-1} = 1.5$  s, the correlation is constant with respect to  $\Delta t$  but increases due to the varying evolution time.

of evolution and delay time for a larger range of delay times up to 100 s. As intended, the autocorrelation function is constant when the sequence probes frequencies between the Lorentzian and high-frequency cutoff. For  $\Delta t \gtrsim \omega_L^{-1}$ , Eq. 7.7 predicts a constant value independent of the delay time. However, the correlation increases again due to the variation of  $\tau$  which goes down to 3 ns at  $\Delta t = 100$  s. Experimentally, measuring the behavior and position of the slope at  $\omega_E^{-1}$  will thus allow to identify the cutoff and its frequency on a measurable scale. The evolution times used for the simulation vary

between 10  $\mu\text{s}$  and 325 ns which is well feasible in experiments.

### 7.3 1/f noise

To illustrate the broad range of applications of the measurement technique I will now consider noise with a spectrum of the form

$$S(\omega) = \frac{S_0}{1 + \left(\frac{\omega}{\omega_C}\right)^\alpha}, \quad (7.9)$$

omnipresent in superconducting qubit systems. Consistent with experiments,  $S_0$  is chosen such that  $\int_0^\infty d\omega S(\omega) = (2\pi \times 10 \text{ MHz})^2$  [31]. The lower cutoff frequency  $\frac{\omega_C}{2\pi} = 1 \text{ Hz}$  has been introduced to avoid numerical divergences at low frequencies. It corresponds to a fluctuation with an oscillation period of 0.16 s which is larger and thus roughly static for any evolution or delay time considered here [31].

As the weight of this spectrum is also concentrated at low frequencies as before, the autocorrelation is determined by  $\chi_-(\tau, \Delta t)$ . Calculating the autocorrelation function for this spectrum to investigate the parameter  $\alpha$  will lead to a variation of  $\chi_-$  over several orders of magnitude whereas deviations due to different  $\alpha$  will be small compared to these scales. I will thus make use of the evolution time to compensate for this variation as in the previous section. For exact  $\frac{1}{\omega}$  noise with  $\alpha = 1$ , this term can be calculated analytically leading to

$$\begin{aligned} \chi_-(\tau, \Delta t) &= \frac{1}{\pi} \left[ 2\tau \Delta t \ln(\Delta t + \tau) - 2\tau \Delta t \ln(\Delta t - \tau) - 2\tau^2 \ln(\tau) - 2\Delta t^2 \ln(\Delta t) \right. \\ &\quad \left. + \Delta t^2 \ln(\Delta t - \tau) + \tau^2 \ln(\Delta t - \tau) + \tau^2 \ln(\Delta t + \tau) + \Delta t^2 \ln(\Delta t + \tau) \right] \\ &\approx \frac{2}{\pi} \tau^2 \ln\left(\frac{\Delta t}{\tau}\right) \end{aligned} \quad (7.10)$$

where  $\tau \ll \Delta t$  was assumed in the second step. A spectrum with  $\alpha < 1$  corresponds to the transition to white noise. This will result in a weaker dependence of  $\chi_-(\tau, \Delta t)$  on the delay time as white noise is equivalent to the absence of correlations. For  $\alpha > 1$ , the dependence on  $\Delta t$  is stronger. To keep the autocorrelation at a measurable level while sweeping the delay time, the evolution time is varied according to

$$\tau = \Delta t e^{W\left(-\frac{2c}{\Delta t^2}\right)} \quad (7.11)$$

where  $W(x)$  is the Lambert W function defined as the solution to  $x = we^w$  [58] and  $c$  is a constant used to set the overall magnitude of  $\chi_-(\tau, \Delta t)$ . Eq. 7.11 can be derived when  $\chi_-(\tau, \Delta t)$  in Eq. 7.10 is set to be constant and will thus lead to a constant autocorrelation

function for  $\alpha = 1$ . Fig. 7.6 illustrates this approach. For  $\alpha = 1$ , the autocorrelation is

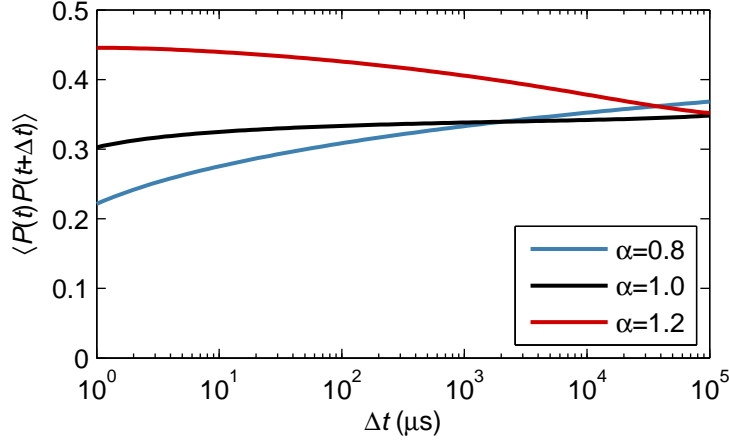


**Figure 7.6:** Autocorrelation for  $1/f^\alpha$  noise with varying evolution time. The slope is characteristic for the respective  $\alpha$ . The deviation from the constant behavior for  $\alpha = 1$  at  $\Delta t \sim 1 \mu\text{s}$  is due to long evolution times compared to the delay time. At  $\Delta t \sim \omega_C^{-1} = 0.15 \text{ s}$  the cutoff is visible also leading to deviations from the constant behavior.

constant over a large range of delay times. The small deviations of this behavior at very short and very long delay times are due to failure of the approximation  $\tau \ll \Delta t$  and the introduced cutoff at  $\Delta t \sim \omega_C^{-1}$ , respectively. Remarkably,  $\alpha < 1$  ( $\alpha > 1$ ) leads to a positive (negative) slope and thus allows to measure this parameter with high sensitivity. The accuracy determining the smallest difference in  $\alpha$  still measurable will be determined by the signal-to-noise ratio which conceals a difference in this parameter in noise fluctuations. The height of the autocorrelation for a fixed  $\tau$  may again be used to determine the overall noise amplitude  $S_0$ . The evolution times used in the simulation lie between 39 ns and 18 ns and thus on an experimentally well feasible scale. Fig. 7.6 shows that using the presented technique allows for investigation and identification of the noise behavior in superconducting qubits over an extremely large range of delay times corresponding to a large range of frequencies.



### Summary

In this part, I have presented a measurement scheme to investigate the dephasing noise spectrum acting on a qubit. The technique relied on using autocorrelations of successive single-shot qubit readout. The independent choice of the evolution and delay time mark its crucial advantage as they allow for tailoring the sequence's sensitivity as required: the evolution time has been shown to set the overall sensitivity whereas the delay time was used to set the frequency region where the sequence is sensitive. Simulations showing the application of the technique to exemplary noise spectra have been presented to investigate the cutoff frequencies of Lorentzian spectra, the expected high-frequency cutoff of Overhauser field fluctuations in electron spin qubits, and also the frequency behavior of  $1/f^\alpha$ -noise in superconducting qubit systems. The simulations indicate that using autocorrelations might indeed outperform pulse sequence-based spectroscopy at investigating these important but yet unobserved properties. Moreover, they reveal the noise spectrum at frequencies that are inaccessible with existing techniques, allowing to probe arbitrarily low frequencies compared to e.g. the lower bound of 0.1 MHz in Ref. [31]. In conclusion, there is strong evidence that this new approach might help to understand the noise acting on a qubit and thus promote techniques to extend coherence times.





## Part III

---

# Probing quantum-mechanics in a spin bath



### Motivation

The laws of quantum mechanics accurately describe physical properties on small length scales and short times. However, these effects cannot be observed in everyday life. This naturally raises the question how the transition between these two worlds takes place: is there a threshold for physical properties below which the system behaves quantum-mechanically and abruptly becomes classically if this limit is exceeded, or is this transition gradual? So far, there is no evidence for a deviation from the quantum-mechanical description of a system for any length scale or time. However, the full quantum-mechanical treatment may not be necessary in certain regimes, e.g. macroscopic objects, where the classical description is sufficient to predict the object's behavior. The link connecting the quantum-mechanical and classical world is decoherence which describes how a system loses its quantum-mechanical properties, e.g. how fast the deterministic, quantum-mechanical state evolves into a mixed state which can be considered classical.

It is both interesting and insightful to probe systems, that are a priori considered classical, for quantum-mechanical properties. Such an experiment has been conducted for example by Arndt et al., who showed that, despite their macroscopic size,  $C_{60}$  fullerenes produce an interference pattern when traversing a small grating [59]. The observation of this purely quantum-mechanical phenomenon shows that also macroscopic objects with many internal degrees of freedom might still reveal properties that are purely quantum-mechanical. Similarly, in superconducting qubits or superconducting quantum interference devices, a large number of electrons can be described by a single macroscopic wave function. Many other experiments in mesoscopic physics aim at pushing the boundary up to which quantum-mechanical behavior is observable. For a review on how to experimentally test the limits of quantum mechanics see Ref. [60].

Following the lines of these kinds of experiments, let us now turn our attention to the electron spin qubit introduced before in which the large nuclear spin bath constitutes a macroscopic system, that has been considered classical in the previous part. Quantum-mechanically, the loss of qubit information is determined by the time scale on which the qubit state entangles with its surrounding noise bath states. It can be regarded as a process during which the information of the qubit diffuses into the environment. While

this entanglement hinders the application for quantum computation and tremendous effort has been made to decouple the qubit from its environment, it makes the qubit a prime candidate to probe its environment. In this part, the electron spin qubit will thus be used to investigate the surrounding nuclear spin bath. More specifically, I will aim at detecting backaction from the electron spin onto the nuclei. While a quantum-mechanical model always includes backaction, simulating a realistic measurement scheme reveals whether the bath can be considered as a classical noise bath (as was assumed in Part II) or if the quantum-mechanical backaction can be detected on a measurable scale. My reasoning is the following: If backaction from the electron spin qubit on the noise bath, manifesting itself in electron spin state-dependent noise bath evolution, is detectable, this indicates that the treatment as a classical noise variable  $\beta(t)$  is invalid and the noise bath behaves quantum-mechanically. To justify this approach, I make use of the fact, that the electron spin is a quantum-mechanical system by definition. If coupling this system to the nuclear spin bath leads to measurable electron spin-dependent noise bath dynamics, this heralds quantum-mechanical behavior of the bath. Due to the large number of  $\sim 10^6$  nuclear spins coupled to the electron, one might a priori assume that the bath acts classically. So far, all experimental results confirm this assumption as classical calculations allow to accurately describe them [13]. Failure of the classical picture in the presented measurement scheme will thus relate to experiments probing quantum-mechanics in macroscopic solid-state systems. Moreover, identification of boundaries above or below which quantum-mechanical results are accurately reproduced by semiclassical calculations will greatly aid theoretical investigations of the spin bath, as neglecting its quantum-mechanical properties crucially facilitates calculations. Though I will only consider electron spins embedded in a GaAs heterostructure, the results are applicable straightforward to e.g. electron spins in self-assembled InGaAs quantum dots.

## Theory

In this chapter, I will lay the foundations to understand the interactions between the electron spin and the nuclear spin bath in the GaAs lattice, which is known as the central spin problem. After introducing this system, I will present the Hamiltonian used for the simulations conducted. Due to their close analogy, I will for simplicity restrict myself to a single electron spin residing in a quantum dot in this chapter and only consider the straightforward extension to the double dot with two electrons when the correlation functions are calculated.

### 10.1 Central spin problem

The electron spin qubit is a prominent example for the realization of the central spin problem: a single electron spin, embedded in a GaAs lattice, is coupled to a bath of fluctuating surrounding spins. This situation is depicted in Fig. 10.1. Although the central spin problem has been known for a long time [61–66], the system has regained a lot of theoretical attention for its potential use in quantum information. The entanglement of the electron spin initialized in a superposition state  $\alpha|\downarrow\rangle + \beta|\uparrow\rangle$  with the nuclear spin bath under the influence of a coupling Hamiltonian  $\hat{H}$  after time  $t$  can be expressed as

$$(\alpha|\downarrow\rangle + \beta|\uparrow\rangle) \otimes |J\rangle \rightarrow \alpha|\downarrow\rangle \otimes |J^\downarrow(t)\rangle + \beta|\uparrow\rangle \otimes |J^\uparrow(t)\rangle, \quad (10.1)$$

where the spin bath state

$$|J\rangle = \otimes_{i=1}^N |j_i\rangle = |\uparrow\downarrow\downarrow\uparrow\downarrow\dots\rangle \quad (10.2)$$

denotes a product of pure states of the  $N$  nuclear spins. The bath is assumed to be unpolarized and uncorrelated, i.e. in an infinite temperature state. To calculate expectation values, different initial nuclear spin bath configurations need to be taken into account via ensemble averaging.  $|J^{\downarrow,\uparrow}(t)\rangle = \otimes_{i=1}^N \exp\left(-\frac{i}{\hbar}\hat{H}^{\downarrow,\uparrow}t\right)|j_i\rangle$  are the nuclear spin states entangled with the respective electron spin state. Qubit coherence can then be expressed as the overlap of the two states  $C(t) \sim |\langle J^\downarrow(t)|J^\uparrow(t)\rangle|$ . Calculation of these overlaps is challenging from a theoretical point of view and different techniques such as a ring diagram

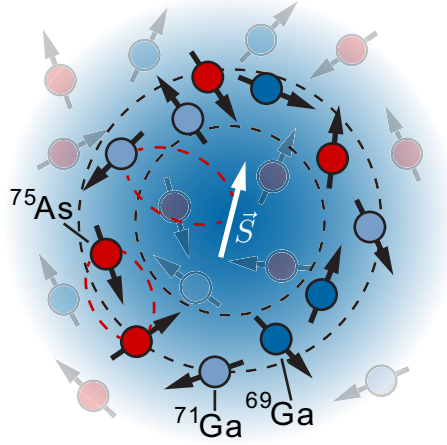


**Figure 10.1:** Illustration of the central spin problem. The electron spin  $\vec{S}$  is coupled to the surrounding nuclear spins ( $^{69}\text{Ga}$ ,  $^{71}\text{Ga}$  and  $^{75}\text{As}$  in a GaAs heterostructure). Interactions (indicated by red, dashed lines) may occur between nuclei and the central electron spin, and nuclei of the same species. Interactions between nuclear spins of different species are suppressed by sufficiently large external magnetic fields. The fading blue area denotes the electron wave function  $|\psi|^2$  weighting the coupling strength of the electron spin to each nuclear spin. The dashed black lines encircle an area containing nuclei with a similar coupling to the electron which will be used to group them into clusters. Transparent nuclear spins have a different hyperfine coupling and thus belong to other clusters. For details see text.

theory [50, 67, 68], a linked-cluster technique [69], and the pair-correlation approximation [39, 70] have been developed to accomplish this task. In the next section, I will focus on the Hamiltonian mediating the entanglement.

## 10.2 Hamiltonian

The Hamiltonian of the central spin problem is given by

$$\begin{aligned}\hat{H} &= \hat{H}_z + \hat{H}_{hf} \\ &= \Omega \hat{S}^z + \sum_i \omega_{L,\alpha[i]} \hat{J}_i^z + \sum_i A_i \mathbf{S} \cdot \mathbf{J}_i\end{aligned}\tag{10.3}$$

where  $\hat{H}_z$  includes the electron and nuclear Zeeman energies  $\Omega$  and  $\omega_{L,\alpha[i]}$ , respectively. The sum over  $i$  runs over all the nuclei coupled to the electron.  $\hat{S}^z$  and  $\mathbf{S}$  ( $\hat{J}_i^z$  and  $\mathbf{J}_i$ ) are electron (nuclear) spin operators and  $\alpha[i]$  denotes the  $i$ th nuclear spin belonging to the nuclear species  $\alpha$ . The Larmor frequencies for the three spin species present in the GaAs lattice  $^{69}\text{Ga}$ ,  $^{71}\text{Ga}$  and  $^{75}\text{As}$  are given in Tab. 10.1. Note that they are roughly equidistant which is an essential prerequisite to observe revivals in the simulations presented below. The intrinsic (electron spin-independent) dipolar interaction was neglected in Eq. 10.3 because only electron spin-dependent dynamics are of interest. Following

**Table 10.1:** Larmor frequencies at  $B = 1$  T and hyperfine energies for isotopes in GaAs [50].

isotope $\alpha$	abundance $n_\alpha$	$\omega_{L,\alpha}$ ( $10^7$ s $^{-1}$ )	$\mathcal{A}_\alpha$ ( $10^{10}$ s $^{-1}$ )	$\mathcal{A}_\alpha$ ( $\mu$ eV)
$^{69}\text{Ga}$	0.4	-6.42	5.47	36
$^{71}\text{Ga}$	0.6	-8.16	6.99	46
$^{75}\text{As}$	1.0	-4.58	6.53	43

Ref. [71], intrinsic interactions can be accounted for through a coherence factor of the form  $\exp\left[-\left(\frac{t}{t_{SD}}\right)^\gamma\right]$  when the number of nuclear spins is large and correlators between different cartesian components of nuclear spins are neglected. The effect of the latter may be introduced phenomenologically by random site-to-site variations of the nuclear Larmor frequencies [71].

The third term denotes interactions between the central electron spin and the surrounding nuclear spins, which will mediate backaction on the nuclear spin bath and is thus the term of interest.  $A_i$  is the hyperfine energy describing this coupling. This energy is weighted by the electron wave function, corresponding to a strong coupling for nuclei close to the electron, whereas distant nuclei are only weakly coupled. For the  $i$ th nucleus, this leads to

$$A_i = \mathcal{A}_{\alpha[i]} \cdot |\psi(\mathbf{r}_i)|^2 \quad (10.4)$$

where  $\mathcal{A}_{\alpha[i]}$  is a species-dependent constant and  $|\psi(\mathbf{r}_i)|^2$  is the electron wave function at the position of the  $i$ th nucleus. Typical values for the three isotopes  $^{69}\text{Ga}$ ,  $^{71}\text{Ga}$  and  $^{75}\text{As}$  together with their respective average abundances per unit cell  $n_\alpha$  are given in Tab. 10.1. The hyperfine term can be rewritten as

$$\hat{H}_{hf} = \sum_i A_i \mathbf{S} \cdot \mathbf{J}_i = \sum_i A_i \left[ \hat{S}^z \hat{J}_i^z + \frac{1}{2} (\hat{S}^+ \hat{J}_i^- + \hat{S}^- \hat{J}_i^+) \right]. \quad (10.5)$$

In the absence of phonons (i.e. at sufficiently low temperatures) and for sufficiently large external magnetic fields, such that  $\Omega \gg A_i$ , the electron-nuclear spin flips are suppressed due to energy conservation. The hyperfine interaction in this so-called secular approximation is given by

$$\hat{H}_{hf} \approx \sum_i A_i \hat{S}^z \hat{J}_i^z \quad (10.6)$$

and will be employed in some of the following calculations.

As described in Eq. 4.5, the hyperfine interaction may be regarded as an effective Overhauser field  $g\mu_B \vec{B}_{nuc} = \sum_i A_i \mathbf{J}_i$ . In this semiclassical picture, the total time-dependent magnetic field in each dot is given by  $|\mathbf{B}_{tot}(t)| = \sqrt{(B_{ext} + B_{nuc}^z)^2 + |\mathbf{B}_{nuc}^\perp(t)|^2}$  where the external magnetic field is assumed to point along the  $z$ -direction. Note that this approach neglects commutators between different components of nuclear spin operators which is a

suitable approximation for large nuclear spin baths as the commutators scale with  $1/N$  [71]. Approximating the field in the limit  $\frac{|\mathbf{B}_{nuc}|}{B_{ext}} \ll 1$ , the hyperfine Hamiltonian can be rewritten as

$$\hat{H}_{hf} \approx g\mu_B \left( B_{nuc}^z + \frac{|\mathbf{B}_{nuc}^\perp|^2}{2|B_{ext}|} \right) \hat{S}^z \quad (10.7)$$

In GaAs, only moderate external fields on the order of a few 10 mT are sufficient for this approximation to hold. The finite perpendicular Overhauser field  $|\mathbf{B}_{nuc}^\perp|$  has two crucial effects. First, it misaligns the quantization axis of the electron spin by an angle  $\theta \sim \frac{|\mathbf{B}_{nuc}|}{|B_{ext}|}$  causing leakage into noncomputational states. Following Ref. [71], this leakage is neglected as it enters the singlet return probability on the order of  $\theta^2$ . The second effect is the modulation of the nuclear Overhauser field leading to the revival behavior in Ref. [13]. This effect is accounted for in Eq. 10.7.



## Measurement scheme

In Part II, autocorrelations of successive free induction decay experiments have been used to gain information about the qubit noise bath, e.g. the magnitude and time evolution of the Overhauser field difference  $\Delta B^z$ . To investigate the quantum-mechanical properties of the bath coupled to the qubit via the autocorrelation function of two projective qubit measurements, I employ a similar approach. The two logical states of the qubit are denoted  $|0\rangle$  and  $|1\rangle$ , respectively. When a superposition  $|-\rangle = \frac{1}{\sqrt{2}}(|0\rangle - |1\rangle)$ , i.e. a  $\hat{\sigma}_x$  eigenstate, is initialized, the autocorrelation function of successive free induction decay experiments is defined as

$$C = \sum_{i,j=\pm 1} i \cdot j \cdot P(i,j) = 2P(-,-) - 2P(+,-) + P(+) - P(-). \quad (11.1)$$

$P(i,j)$ , where  $i,j \in [+, -]$ , denotes the probability to measure the outcome  $i$  after the first free induction decay and the outcome  $j$  in the second measurement. Note that  $P(i,j)$  are projective measurements  $|\langle \pm | \psi \rangle|^2$  where  $|\psi\rangle$  is the qubit state at the time of the measurement.  $P(\pm)$  denotes the measurement outcome of the first measurement. Rescaling the autocorrelation function by omitting these uninteresting terms and the factor 2 leads to a simpler expression for the autocorrelation that will be used for the calculations below

$$C = P(-,-) - P(+,-). \quad (11.2)$$

If the two readouts are uncorrelated, the measurement outcome of the second FID is independent of the first and thus  $C = 0$ . For a process illustrated in Fig. 5.1, the state of the qubit coupled to the noise bath after the first FID of duration  $t_1$  is given by

$$|\psi\rangle = \frac{1}{2}|-\rangle \otimes (U_0(t_1)|J\rangle + U_1(t_1)|J\rangle) + \frac{1}{2}|+\rangle \otimes (U_0(t_1)|J\rangle - U_1(t_1)|J\rangle) \quad (11.3)$$

where  $|\pm\rangle$  are the qubit superposition states,  $|J\rangle$  is the noise bath state and  $U_{0,1}(t)$  are unitary operators mediating the entanglement of the noise bath state with the qubit states. A strong measurement with the outcome  $|\pm\rangle$  projects the bath state onto a superposition

state  $\frac{1}{\sqrt{\langle\phi|\phi\rangle}} (U_0|J\rangle \mp U_1|J\rangle)$ . The normalization of this state is given by

$$\begin{aligned}\langle\phi|\phi\rangle &= \langle J(U_0(t_1) \mp U_1(t_1)) | (U_0(t_1) \mp U_1(t_1))J \rangle \\ &= 2 \mp \langle J|U_0^\dagger(t_1)U_1(t_1)|J\rangle \mp \langle J|U_1^\dagger(t_1)U_0(t_1)|J\rangle \\ &\approx 2.\end{aligned}\tag{11.4}$$

Note that overlaps  $\langle J|U_0^\dagger(t_1)U_1(t_1)|J\rangle$  have been neglected in the last step as they decay on a FID time scale, which is much faster than typical time scales for autocorrelation measurements. The state of the system after the second FID of duration  $t_2$  is given by

$$\begin{aligned}|\psi^\pm\rangle &= \frac{1}{2}|0\rangle \otimes [U_0(t_2)U_I(\Delta t)U_0(t_1) \mp U_0(t_2)U_I(\Delta t)U_1(t_1)]|J\rangle \\ &\quad - \frac{1}{2}|1\rangle \otimes [U_1(t_2)U_I(\Delta t)U_0(t_1) \mp U_1(t_2)U_I(\Delta t)U_1(t_1)]|J\rangle,\end{aligned}\tag{11.5}$$

where  $\Delta t$  is the duration of the idle (or intermediate) time in between the two FIDs.  $U_I(\Delta t)$  is the corresponding evolution operator containing the dynamics of the system during this time. The superscript  $|\psi^\pm\rangle$  denotes the single-shot outcome  $|\pm\rangle$  of the first measurement.  $P(i, j)$  in Eq. 11.2 can now be calculated via the overlaps of the nuclear spin states of  $|\psi^\pm\rangle$  entangled with the two qubit states leading to

$$C = \frac{1}{2} \left( \langle J | \underbrace{U_0^\dagger U_I^\dagger U_0^\dagger U_1 U_I U_1}_{FID} | J \rangle + \langle J | \underbrace{U_1^\dagger U_I^\dagger U_0^\dagger U_1 U_I U_0}_{SE} | J \rangle \right).\tag{11.6}$$

The two terms in this expression are identical to coherence functions of a free induction decay and a spin echo, respectively [50], when  $U_I(\Delta t) \sim 1$ , e.g. because  $\Delta t$  is short compared to the energy scales of the interactions. If  $U_I$  commutes with the two coupling operators  $U_0$  and  $U_1$ , the exact equivalence to the FID and SE coherence holds even for arbitrarily long intermediate evolution times  $\Delta t$ . For a single electron in a quantum dot coupled to a bath of nuclear spins as defined in Eq. 10.2,  $|J\rangle = \otimes_i^N |j_i\rangle$ , where the  $|j_i\rangle$  are pure states of the nuclear spins. To calculate expectation values, averaging over the nuclear spin ensemble is required.  $U_{0,1} = U_{\downarrow,\uparrow} = e^{-\hat{H}_{hf}^{\downarrow,\uparrow} t}$  are the unitary evolution operators coupling each nucleus to the electron spin where  $\hat{H}_{hf}^{\downarrow,\uparrow}$  is the Hamiltonian in Eq. 10.5 associated to the electron states  $|\downarrow\rangle$  and  $|\uparrow\rangle$ . In the double dot configuration (for the singlet triplet qubit),  $|J\rangle = |J_L\rangle \otimes |J_R\rangle$  where  $|J_{L,R}\rangle$  denotes the nuclear spin states in the left and right dot, respectively. In this case, the evolution operators are associated to the qubit states  $|\uparrow\downarrow\rangle$  and  $|\downarrow\uparrow\rangle$  leading to  $U_0 = U_\uparrow \otimes U_\downarrow$  ( $U_1 = U_\downarrow \otimes U_\uparrow$ ). If the nuclear spin baths in the two dots are assumed to be independent, i.e. operators acting on different baths commute, the autocorrelation function for the singlet triplet qubit is composed of

factors each including contributions from only one dot

$$C = \frac{1}{2} \left[ \langle J_L | U_{\downarrow}^{\dagger} U_I^{\dagger} U_{\downarrow}^{\dagger} U_{\uparrow} U_I U_{\uparrow} | J_L \rangle \langle J_R | U_{\uparrow}^{\dagger} U_I^{\dagger} U_{\uparrow}^{\dagger} U_{\downarrow} U_I U_{\downarrow} | J_R \rangle \right. \\ \left. + \langle J_L | U_{\uparrow}^{\dagger} U_I^{\dagger} U_{\uparrow}^{\dagger} U_{\downarrow} U_I U_{\downarrow} | J_L \rangle \langle J_R | U_{\downarrow}^{\dagger} U_I^{\dagger} U_{\downarrow}^{\dagger} U_{\uparrow} U_I U_{\uparrow} | J_R \rangle \right]. \quad (11.7)$$

Remarkably, even in a quantum-mechanical treatment, the autocorrelation function is identical to expressions describing the coherence of a free induction decay and a spin echo experiment when  $[U_I, U_{\uparrow}] = [U_I, U_{\downarrow}] = 0$ . Note the close similarity to the results in Part II, where the filter functions of the autocorrelation resembled that of free induction and spin echo decays. Measuring this function will thus not give insights into the quantum-mechanical properties of the nuclear spin bath beyond that of coherence measurements. To overcome this problem, I consider the following two measurement schemes based on the implementation of noncommuting evolutions, which will be used to notably change the state of the nuclei due to interactions with the electron spin. The schemes are similar in the sense that they consist of two evolutions followed by projective measurements. In between these measurements, different approaches to realize a noncommuting bath evolution are proposed. The second projective measurement will then implicitly measure the effect of this intermediate noncommuting evolution. Though the two measurement operators are identical and thus commute, calculating their autocorrelation allows to detect the change of the bath caused by the intermediate evolution, i.e. the backaction from the electron spin on the nuclear spin bath.

It is important to note that a decay of this correlation due to backaction is significantly different from coherence measurements. For the latter, the loss of coherence can be reduced to an inhomogeneous broadening process, when the bath is assumed to be in an infinite temperature state. This approximation is suitable in GaAs as the nuclear Larmor frequencies in Tab. 10.1 correspond to temperatures less than 1 mK which is well below typical cryostat operating temperatures of  $\sim 100$  mK. Due to the nature of the resulting nuclear bath density matrix, there is always a basis in which the coupling Hamiltonian is diagonal. Consider for example a single electron in a FID. The coherence is given by

$$\sum_J P_J \left| \langle J | U_{\uparrow}^{\dagger} U_{\downarrow} | J \rangle \right| e^{i\phi_J} \xrightarrow{T \rightarrow \infty} \sum_J P_J e^{i\phi_J}, \quad (11.8)$$

where  $P_J$  is the thermal distribution factor denoting the probability of each noise bath configuration  $J$ , and  $\phi_J$  is a phase containing the electron Zeeman splitting and its shift due to the Overhauser field [39]. In the second step, I chose a basis for  $|J\rangle$  such that the evolution operators are diagonal in this basis, leading to a phase that vanishes due to the absolute value. The resulting expression is an average over the phase  $\phi_J$  which is equivalent to an inhomogeneous broadening process. The decay of coherence can thus

be regarded as a smearing out of a phase. Correlations of noncommuting measurements, however, directly measure the backaction effect of the electron on the nuclear spins, which cannot be expressed as a simple phase and is thus in stark contrast to a  $T_2^*$  process.

The first measurement scheme relies on a rotation of the external magnetic field. However, this will be experimentally challenging and rather serves as a simple example to illustrate the effects of the noncommuting evolutions, hence it will be called toy model in the following. The second scheme is experimentally feasible and describes a realistic approach to detect backaction from the electron spin on the nuclear spin bath by comparing free induction decay and spin echo evolutions.

## 11.1 Toy model scheme

The measurement scheme for the toy model is depicted in Fig. 11.1. It comprises two initialization-evolution-measurement cycles of duration  $t_1$  and  $t_2$ , respectively, as in Chapter 5. The initialized state for those two is  $|S(1,1)\rangle$ . Again, initialization and measurement are assumed to be negligibly short. In between, the qubit is initialized into either  $|\uparrow\downarrow\rangle$ ,  $|\downarrow\uparrow\rangle$  or the  $|T_+(1,1)\rangle$  state and evolves for a time  $\tau$  without subsequent measurement. During the first and third evolution, the external magnetic field is aligned along the  $z$ -

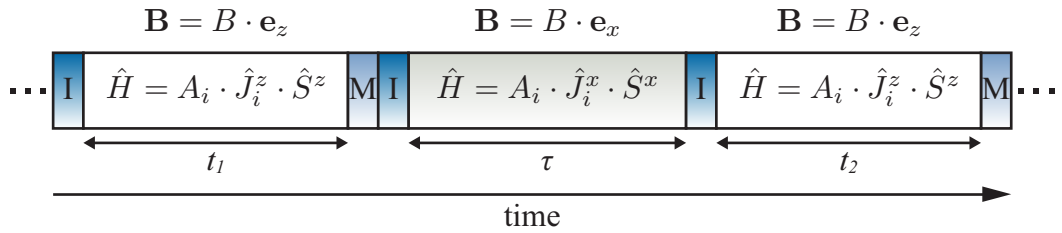


**Figure 11.1:** Measurement sequence for the toy model scheme. It consists of three free evolutions during which the hyperfine interaction couples the electron spin to the nuclei. The qubit is initialized (I) in the singlet (first and third evolution) and either  $|\uparrow\downarrow\rangle$ ,  $|\downarrow\uparrow\rangle$  or the  $|T_+(1,1)\rangle$  for the second evolution. A projective measurement (M) is applied after the first and third evolution of duration  $t_1$  and  $t_2$ , respectively. During these evolutions, the external magnetic field points along the  $z$ -axis and thus couples the qubit to the  $z$ -component of each nuclear spin. During the second evolution of duration  $\tau$ , it is rotated into the  $x$ -direction, effectively coupling the electron spin to the  $x$ -component of each nuclear spin. The hyperfine interaction between the electron and the nuclei is given in each box denoting the respective evolution.

direction. Before the second evolution, it is rotated into the  $x$ -direction, effectively rotating the quantization axis of the electron spin and thus coupling the electron spin to the  $\hat{J}_i^x$  component of the nuclei. As  $\hat{J}_i^z$  and  $\hat{J}_i^x$  do not commute, this rotation of the external magnetic field corresponds to noncommuting nuclear spin evolutions. The measurement outcomes then allow to compute the autocorrelation function as a function of  $t$  and  $\tau$ .

While the rotation of external magnetic fields is possible with vector magnets, the time scale of such adjustments is much larger than typical qubit evolution times. This makes the presented measurement scheme experimentally infeasible and the simulations predicting its autocorrelation function will rather serve as a simple example to gain insights into the effects of backaction.

## 11.2 Pulse scheme

The pulse scheme relies on the different effects of a free induction decay and a spin echo experiment on the nuclear spin bath. For the latter, the backaction from the electron on the nuclei is reversed as the application of a  $\pi$ -pulse can be considered as inverting the sign of the hyperfine interaction in the middle of the evolution. The free induction decay, however, will have a nonzero backaction. The measurement scheme is illustrated in Fig. 11.2. Instead of rotating the magnetic field between the two initialization-evolution-measurement cycles, a third evolution is included with an optional  $\pi$ -pulse in the middle. This corresponds to either a free induction decay or a spin echo, and differences in the autocorrelation function for those two cases will thus indicate a significant backaction from the electron on the nuclear spin bath. The free induction decay is sensitive to the constant

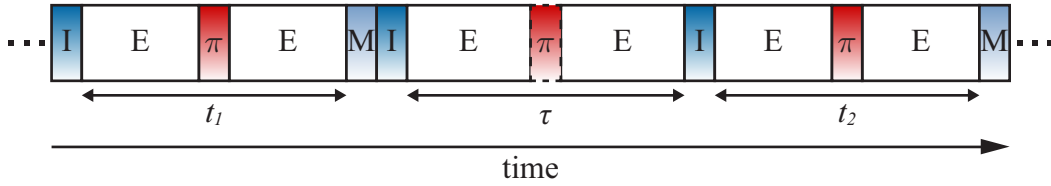


**Figure 11.2:** Measurement sequence for the pulse scheme. It consists of two initialization-spin echo-measurement cycles, denoted I, E and M, respectively, framing a third evolution that is either a free induction decay or a spin echo.  $\pi$ -pulses are applied in the middle of each evolution as illustrated by the red boxes.

$z$ -component of the Overhauser field  $B_{nuc}^z \sim \hat{I}^z$  whereas in a spin-echo experiment, this component cancels out and only the relative phases of the time-dependent transverse Overhauser field components  $B_{nuc}^\perp \sim \hat{I}^\pm$  created by the three different nuclear spin species have an effect [71]. The free induction decay embedded into the two spin echo measurements can thus be regarded as a noncommuting evolution as  $[\hat{I}^z, \hat{I}^\pm] \neq 0$ . I assume that the duration for initialization, measurement and the application of the  $\pi$ -pulse are negligibly short (the so called bang-bang limit). In principle, one could also use free induction decays for the outer evolutions. However, it would then be necessary to consider that through the backaction during the intermediate evolution, also the longitudinal Overhauser field component will be changed and affect the second measurement. This effect is not included

in the model presented below and I will thus restrict myself to spin echo experiments as outer evolutions.

## Calculation of correlation function

### 12.1 Toy model scheme

The calculation of the autocorrelation function for the toy model scheme will be presented below. In order to take into account the large number of nuclear spins on the order of  $10^6$ , I will employ two different approaches. The first can be regarded as a semiclassical approximation in which each nuclear spin is treated as a classical vector. This is motivated by the success of the semiclassical calculations in Ref. [71], that reproduced an effective Hamiltonian for the spin echo coherence derived previously in Ref. [50], where a Schrieffer-Wolff transformation was used, and accurately described the experimental results in Ref. [13]. The second approach respects the quantum-mechanical nature of the nuclear spin bath. Comparison of the simulations for the two approaches in the following chapter will thus reveal whether the semiclassical treatment suffices to describe the autocorrelation of the two measurements. For the toy model scheme, the secular approximation introduced in Eq. 10.6 will be applied.

#### 12.1.1 Semiclassical approach

The readout of the two measurements, which is defined as the probability to measure the initialized singlet state, is determined by the difference of the Overhauser fields in the two dots

$$P(t) = \frac{1}{2} \left[ 1 + \cos \left( \frac{g\mu_B}{\hbar} \Delta B^z t \right) \right]. \quad (12.1)$$

If measuring a singlet (triplet) state is associated with the result  $+1$  ( $-1$ ), the probability to measure the outcome  $\alpha = \pm 1$  in the second measurement and the outcome  $\beta = \pm 1$  in the first measurement is given by

$$P(\alpha, \beta) = \frac{1}{2} (1 + \alpha \cdot \cos(\tilde{\omega}^z t_2)) \cdot \frac{1}{2} (1 + \beta \cdot \cos(\omega^z t_1)), \quad (12.2)$$

where  $\omega^z = \frac{g\mu_B}{\hbar} \Delta B^z$  ( $\tilde{\omega}^z = \frac{g\mu_B}{\hbar} \Delta \tilde{B}^z$ ), the tilde denotes the nuclear spin bath configuration during the second measurement and  $t_{1,2}$  are the durations of the first and third evolution as depicted in Fig. 11.1. The autocorrelation of the two measurements can then be written as

$$C = \sum_{\alpha, \beta = \pm 1} \alpha \cdot \beta \cdot P(\alpha, \beta) = \cos(\tilde{\omega}^z t_2) \cdot \cos(\omega^z t_1). \quad (12.3)$$

The Overhauser field difference  $\Delta B^z$  may be expressed via the contribution of each nuclear spin coupled to the central electron in the respective dots

$$\Delta B^z = B_{nuc,L}^z - B_{nuc,R}^z = \sum_i^{N_L} (A_i J_i^z) - \sum_j^{N_R} (A_j J_j^z) \quad (12.4)$$

where the  $N_{L,R}$  denote the total number of nuclear spins in the left and right dot, respectively and  $A_i$  is the hyperfine coupling in units of  $s^{-1}$ .

To determine the coupling strength for each nucleus, I take the weighting due to the electron wave function into account. When the number of nuclei is large, a continuous density of hyperfine couplings  $\rho_\alpha(A)$  can be calculated leading to

$$\rho_\alpha(A) = \frac{3N}{2\pi A} \arccos \left[ \sqrt{\frac{3NA}{8A_\alpha}} \Theta \left( \frac{8A_\alpha}{3N} - A \right) \right]. \quad (12.5)$$

The normalization for this function is  $\int_0^{\frac{8A_\alpha}{3N}} \rho_\alpha(A) \cdot A dA = \mathcal{A}_\alpha$ . Eq. 12.5 has been introduced in Ref. [50] and implies an electron wave function consisting of a cosine in the  $z$ -direction and a Gaussian in the  $x$ - and  $y$ -direction resulting from the confinement of the 2DEG stemming from the heterostructure and the roughly parabolic potential created by the gates on top of the structure, respectively (see Fig. 2.2).  $\Theta(x)$  is the Heaviside step function. The wave function in the  $z$ -direction is in principle given by an Airy function. However, numerical calculations show that using a cosine instead is a good approximation. The density function allows to calculate how many spins with a specific hyperfine coupling are coupled to the electron spin. This is depicted in Fig. 12.1. The strength of the hyperfine coupling scales inversely with the number of nuclei which results from a larger spread of the electron wave function if many nuclei are coupled. This leads to a dependence  $T_2^* \propto \frac{1}{\sqrt{N}}$  when the nuclear spin fluctuations are assumed to be Gaussian. This dependence agrees very well to the relationship of the reported values  $T_2^* \sim 2$  ns for InGaAs double quantum dots with typically  $N \sim 10^4$  [72] and  $T_2^* \sim 10$  ns for GaAs double quantum dots with  $N \sim 10^6$  [12] without external magnetic field. If not specified otherwise,  $A_i \in \left[0, \frac{8A_\alpha}{3N}\right]$  will be discretized into 5 equidistant segments for the calculations below, effectively creating 15 clusters for the three different spin species where all the spins in one cluster have a similar coupling strength as indicated in Fig. 10.1. The number of



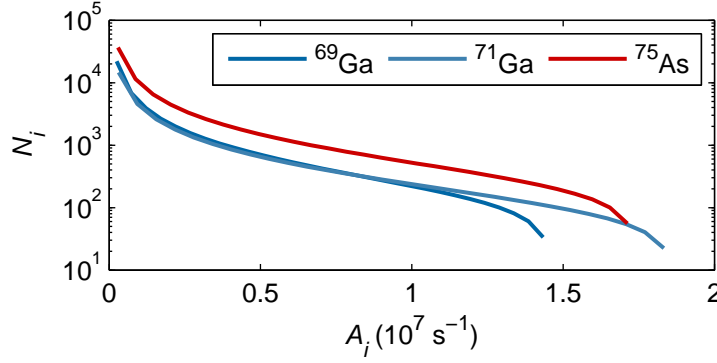


**Figure 12.1:** Distribution of hyperfine couplings for the three nuclear spin species  $^{69}\text{Ga}$ ,  $^{71}\text{Ga}$  and  $^{75}\text{As}$  described in Eq. 12.5 for  $N = 10^6$  and  $A_\alpha$  given in Tab. 10.1. The coupling of the majority of spins is negligible and only a few are coupled strongly to the electron. While the hyperfine energies for the three spin species are similar, there are more spins for  $^{75}\text{As}$  (red curve) due to the higher abundance  $n_{\alpha[i]}$ .

spins in each cluster is then given by

$$N_i = \rho(A_i) \cdot n_{\alpha[i]} \cdot dA, \quad (12.6)$$

where  $\rho(A_i)$  is the hyperfine distribution function in Eq. 12.5,  $n_{\alpha[i]}$  is the abundance of the nuclear spin species  $\alpha$  and  $dA$  is the width of the bins into which the hyperfine coupling has been discretized. The spin quantum numbers for the three nuclear spin types is  $\frac{3}{2}$ . For simplicity, I will however assume nuclear spins  $\frac{1}{2}$  in the following. Note that this is yet not a general limitation for the calculations presented below.

When the nuclear spins are considered as independent, random three-dimensional vectors, the intermediate evolution in the modified magnetic field effectively rotates each spin by an amount determined by the strength of its coupling to the electron about the  $x$ -axis. This transformation may be written as

$$\begin{aligned} \tilde{J}_i^x &= J_i^x \\ \tilde{J}_i^y &= \cos\left(\frac{A_i}{2} J_i^x \tau\right) J_i^y + \sin\left(\frac{A_i}{2} J_i^x \tau\right) J_i^z \\ \tilde{J}_i^z &= \cos\left(\frac{A_i}{2} J_i^x \tau\right) J_i^z - \sin\left(\frac{A_i}{2} J_i^x \tau\right) J_i^y. \end{aligned} \quad (12.7)$$

Note that this semiclassical treatment neglects commutators of the form  $[J_i^\alpha, J_i^\beta]$  with  $\alpha, \beta \in [x, y, z]$  but takes into account the quantum-mechanical hyperfine interaction. Plug-

ging the rotated nuclear spins into Eq. 12.3 and averaging leads to

$$\begin{aligned}
 \langle C \rangle &= \left\langle \cos \left[ \left( \sum_i^{N_L} A_i \tilde{J}_i^z - \sum_j^{N_R} A_j \tilde{J}_j^z \right) t_2 \right] \cdot \cos \left[ \left( \sum_i^{N_L} A_i J_i^z - \sum_j^{N_R} A_j J_j^z \right) t_1 \right] \right\rangle \\
 &= \frac{1}{4} \left\langle \left( e^{i \sum_i^{N_L} A_i (J_i^z t_1 + \tilde{J}_i^z t_2)} \cdot e^{-i \sum_j^{N_R} A_j (J_j^z t_1 + \tilde{J}_j^z t_2)} \right. \right. \\
 &\quad \left. \left. + e^{i \sum_i^{N_L} A_i (J_i^z t_1 - \tilde{J}_i^z t_2)} \cdot e^{-i \sum_j^{N_R} A_j (J_j^z t_1 - \tilde{J}_j^z t_2)} + c.c. \right) \right\rangle, \quad (12.8)
 \end{aligned}$$

where  $\langle \dots \rangle$  denotes ensemble averaging over the initial bath state configuration. I will now assume that the distance between the two dots is sufficiently large so that interactions between nuclei in different dots are negligible and the two nuclear spin baths may be considered independent. In experiments, typical distances of the dots lie on the order of  $\gtrsim 50$  nm. For simplicity, I will assume  $t_1 = t_2 = t$  as in the previous part, and that the two dots are identical which implies identical electron wave functions and thus number of nuclei so that  $N_L = N_R = N$ . Using this approximation, the correlation function may be simplified to

$$\begin{aligned}
 \langle C \rangle &= \frac{1}{2} \left| \left\langle e^{i \sum_i^N A_i (J_i^z + \tilde{J}_i^z) t} \right\rangle \right|^2 + \frac{1}{2} \left| \left\langle e^{i \sum_i^N A_i (J_i^z - \tilde{J}_i^z) t} \right\rangle \right|^2 \\
 &= \frac{1}{2} \prod_i^N \left| \left\langle e^{i A_i \left[ \left( 1 + \cos\left(\frac{A_i}{2} J_i^x \tau\right) \right) J_i^z - \sin\left(\frac{A_i}{2} J_i^x \tau\right) J_i^y \right] t} \right\rangle \right|^2 \\
 &\quad + \frac{1}{2} \prod_i^N \left| \left\langle e^{i A_i \left[ \left( 1 - \cos\left(\frac{A_i}{2} J_i^x \tau\right) \right) J_i^z - \sin\left(\frac{A_i}{2} J_i^x \tau\right) J_i^y \right] t} \right\rangle \right|^2. \quad (12.9)
 \end{aligned}$$

While the results above were derived for the singlet-triplet qubit consisting of two quantum dots each containing one electron, the case of a single quantum dot with one electron coupled to a nuclear spin bath, i.e. the original central spin configuration, can again be calculated by simply dropping the square of the absolute value in the equations above. To perform the average, each nuclear spin  $\mathbf{J}_i$  will be treated as a random vector with a Gaussian distribution

$$P(\mathbf{J}_i) = \frac{1}{\sqrt{2\pi}\sigma^2} \exp \left[ -\frac{1}{2} \left( \frac{\mathbf{J}_i}{\sigma} \right)^2 \right] \quad (12.10)$$

in  $x$ ,  $y$  and  $z$  direction. The variance is determined by the spin quantum number of each nuclear spin  $J^2 = j(j+1) = \frac{3}{4}$ . Distributing this fluctuation among  $J^x$ ,  $J^y$  and  $J^z$  leads to  $\sigma = \frac{1}{2}$ . Note that this assumption does not conserve the total spin length which is motivated by the large number of fluctuating nuclear spins. Integrating the  $y$ -

and  $z$ -component in Eq. 12.9 leads to

$$\begin{aligned} \langle C \rangle &= \frac{1}{2} \prod_{i=1}^N \left( \int_{-\infty}^{\infty} dJ_i^x \frac{1}{\sqrt{2\pi\sigma^2}} e^{-\frac{1}{2}\left(\frac{J_i^x}{\sigma}\right)^2} e^{-2A_i^2\sigma^2 \cos^2\left(\frac{A_i}{4}J_i^x\tau\right)t^2} \right)^2 \\ &+ \frac{1}{2} \prod_{i=1}^N \left( \int_{-\infty}^{\infty} dJ_i^x \frac{1}{\sqrt{2\pi\sigma^2}} e^{-\frac{1}{2}\left(\frac{J_i^x}{\sigma}\right)^2} e^{-2A_i^2\sigma^2 \sin^2\left(\frac{A_i}{4}J_i^x\tau\right)t^2} \right)^2. \end{aligned} \quad (12.11)$$

The remaining integration over each  $J_i^x$  needs to be calculated numerically. Similar to Part II, the first term is typically negligible for small evolution times  $A_i\tau \lesssim 1$  and small evolution times  $t$  due to its large exponent whereas the second term may lead to a significant contribution. To take into account inhomogeneous coupling, I make use of the distribution function of  $A_i$  given in Eq. 12.5. The discretization of the coupling into  $n$  clusters leads to

$$\begin{aligned} \langle C \rangle &= \frac{1}{2} \prod_{i=1}^n \left( \int_{-\infty}^{\infty} dJ_i^x \frac{1}{\sqrt{2\pi\sigma^2}} e^{\frac{1}{2}\left(\frac{J_i^x}{\sigma}\right)^2} e^{-A_i^2\sigma^2 \cos^2\left(\frac{A_i}{4}J_i^x\tau\right)t^2} \right)^{2N_i} \\ &+ \frac{1}{2} \prod_{i=1}^n \left( \int_{-\infty}^{\infty} dJ_i^x \frac{1}{\sqrt{2\pi\sigma^2}} e^{\frac{1}{2}\left(\frac{J_i^x}{\sigma}\right)^2} e^{-A_i^2\sigma^2 \sin^2\left(\frac{A_i}{4}J_i^x\tau\right)t^2} \right)^{2N_i}, \end{aligned} \quad (12.12)$$

where  $N_i$  denotes the number of nuclear spins in each cluster as defined in Eq. 12.6.

### 12.1.2 Quantum-mechanical approach

In the previous calculations, the correlation function was derived using a semiclassical approach that treated the nuclear spins as independent random vectors. To check the validity of this approach, a quantum-mechanical treatment will be used that takes into account the quantization of the nuclei. The correlation as defined in Eq. 11.7 may be calculated by replacing  $U_I(\Delta t)$  with the corresponding evolution operator in Eq. 11.5 to include an evolution of the nuclear spins about the  $x$ -axis resulting from the rotation of the electron's quantization axis. Note that for the calculations below the initialized state for the intermediate evolution is  $|\uparrow\downarrow\rangle$ . However, initialization into  $|\downarrow\uparrow\rangle$  or one of the doubly polarized states leads to the same results. The correlation function is given by

$$\begin{aligned} C &= \frac{1}{2} \left( \langle J_L | U_-^{z\dagger} U_+^{x\dagger} U_-^{z\dagger} U_+^x U_+^z | J_L \rangle \langle J_R | U_+^{z\dagger} U_-^{x\dagger} U_+^{z\dagger} U_-^x U_-^z | J_R \rangle \right. \\ &+ \left. \langle J_L | U_+^{z\dagger} U_+^{x\dagger} U_-^{z\dagger} U_+^x U_+^z | J_L \rangle \langle J_R | U_-^{z\dagger} U_-^{x\dagger} U_+^{z\dagger} U_-^x U_+^z | J_R \rangle \right) \\ &= \frac{1}{2} \langle J_L | U_L' | J_L \rangle \langle J_R | U_R' | J_R \rangle + \frac{1}{2} \langle J_L | U_L'' | J_L \rangle \langle J_R | U_R'' | J_R \rangle. \end{aligned} \quad (12.13)$$

As only electron-spin dependent nuclear spin interactions are of interest, the evolution operators are given by  $U_{\pm}^{z,x}(t) = \otimes_i^N \exp\left(\mp i \frac{1}{2} A_i J_i^{z,x} t\right)$  and only include the hyperfine interaction in the secular approximation. Note that  $U_d' = \otimes_i^N U_{d,i}'$  ( $U_d'' = \otimes_i^N U_{d,i}''$ ), where  $d = L, R$  denotes the left and right dot, respectively, are products of evolution operators acting on each nuclear spin. Again,  $|J_{L,R}\rangle$  denotes the bath states in the two dots. The  $\pm$  is associated to the electron spin state in each dot ( $|\uparrow\rangle$  or  $|\downarrow\rangle$ ). Note that Eq. 12.13 is general in the sense that it allows to calculate the correlation of the two measurements with any other evolution embedded into the two outer evolutions by replacing  $U_{\pm}^x(\tau)$  with the corresponding operator. The correlator again consists of the product of factors each involving one nuclear spin. Calculating  $U_{L,i}'$  and  $U_{L,i}''$  for a single nuclear spin  $|j_i\rangle$  sitting in the left dot leads to

$$\begin{aligned}\langle \uparrow_i | U_{L,i}' | \uparrow_i \rangle &= e^{-i \frac{A_i}{2} t_1} \left[ -2i \sin\left(\frac{A_i}{2} t_2\right) \cos^2\left(\frac{A_i}{4} \tau\right) + e^{i \frac{A_i}{2} t_2} \right] \\ \langle \uparrow_i | U_{L,i}'' | \uparrow_i \rangle &= e^{i \frac{A_i}{2} t_1} \left[ -2i \sin\left(\frac{A_i}{2} t_2\right) \cos^2\left(\frac{A_i}{4} \tau\right) + e^{i \frac{A_i}{2} t_2} \right].\end{aligned}\quad (12.14)$$

It can be shown, that

$$\begin{aligned}\langle \uparrow_i | U_{L,i}' | \uparrow_i \rangle &= \left( \langle \downarrow_i | U_{L,i}' | \downarrow_i \rangle \right)^* = \left( \langle \uparrow_i | U_{R,i}' | \uparrow_i \rangle \right)^* \\ \langle \uparrow_i | U_{L,i}'' | \uparrow_i \rangle &= \left( \langle \downarrow_i | U_{L,i}'' | \downarrow_i \rangle \right)^* = \left( \langle \uparrow_i | U_{R,i}'' | \uparrow_i \rangle \right)^*.\end{aligned}\quad (12.15)$$

To calculate the autocorrelation function, the hyperfine distribution function in Eq. 12.5 is now discretized analogous to the previous section into  $n$  different couplings. To average over the nuclear spin distribution, all possible configurations of the nuclear spins ( $|\uparrow\rangle$ ,  $|\downarrow\rangle$ ) within each cluster are averaged over according to a binomial distribution. This implies that the individual spins are not correlated among each other. The nuclear spin bath is assumed to be unpolarized so that the probability for the binomial distribution is  $\frac{1}{2}$  and the number of spins in each cluster is  $N_i$ . The autocorrelation function is then given by

$$\begin{aligned}\langle C \rangle &= \frac{1}{2} \left( \prod_{i=1}^n \left| \sum_{k=1}^{N_i} \frac{1}{2^{N_i}} \binom{N_i}{k} \left[ \langle \uparrow | U_{L,i}' | \uparrow \rangle \right]^k \left[ \langle \downarrow | U_{L,i}' | \downarrow \rangle \right]^{N_i-k} \right|^2 \right. \\ &\quad \left. + \prod_{i=1}^n \left| \sum_{k=1}^{N_i} \frac{1}{2^{N_i}} \binom{N_i}{k} \left[ \langle \uparrow | U_{L,i}'' | \uparrow \rangle \right]^k \left[ \langle \downarrow | U_{L,i}'' | \downarrow \rangle \right]^{N_i-k} \right|^2 \right),\end{aligned}\quad (12.16)$$

where the sum over  $k$  runs over the number of nuclear spins in each cluster in a  $|\uparrow\rangle$  state and the product over the index  $i$  runs over the different hyperfine couplings. The formalism also allows to include polarized spin baths by adjusting  $p$ . For large  $N$ , such that the number of spins per cluster is large, the binomial distribution may be replaced

by a Gaussian distribution with mean  $\frac{1}{2}N_i$  and variance  $\frac{1}{4}N_i$ .

## 12.2 Pulse scheme

For the experimentally more relevant pulse scheme, I will apply and briefly review the formalism introduced in Ref. [71]. The secular approximation will be dropped and I consider the Hamiltonian defined in Eq. 10.7. However, electron-nuclear spin flip-flops are still neglected. Analogous to Eq. 12.3, the correlation function is given by

$$\langle C \rangle = \langle \cos(\Delta\phi) \cos(\Delta\phi') \rangle \quad (12.17)$$

where  $\Delta\phi = \phi_L - \phi_R$  ( $\Delta\phi' = \phi'_L - \phi'_R$ ) denotes the phase difference of the electron in the left and right dot at the first (second) measurement. Again,  $\langle \dots \rangle$  denotes averaging over the initial Overhauser field configurations. When the dots are independent, this expression can be simplified to

$$\langle C \rangle = \frac{1}{2} \Re \left( \left\langle e^{i(\phi_L + \phi'_L)} \right\rangle \left\langle e^{-i(\phi_R + \phi'_R)} \right\rangle + \left\langle e^{i(\phi_L - \phi'_L)} \right\rangle \left\langle e^{-i(\phi_R - \phi'_R)} \right\rangle \right), \quad (12.18)$$

where  $\Re$  denotes the real part of the expression. The phases are determined by the Overhauser field that the electrons in the dots experience during their evolution. For spin echo experiments, the longitudinal Overhauser field component  $B_{nuc}^z$  cancels out and the two measurements are thus solely determined by the time-dependent transverse field  $|\mathbf{B}_{nuc,d}^\perp(t)|^2 = \sum_{k,l} b_{k,d}(t) b_{l,d}^*(t)$ . The sum runs over the  $n$  different spin species and hyperfine couplings in the respective dot. Its components can be expressed in the complex plane as

$$b_{k,d}^\sigma(t) = \frac{A_k}{g\mu_B} \left[ \overline{I_{k,d}^{\sigma x}(t)} + i \overline{I_{k,d}^{\sigma y}(t)} \right] = b_{k,d}(0) e^{i\omega_k t + i\sigma A_k \int_0^t dt' c(t')}, \quad (12.19)$$

where the time evolution of each Overhauser field component is determined by its Larmor precession and the backaction from the electron spin.  $\overline{I_{k,d}^{\sigma x,y}(t)}$  are the expectation values of the transverse components of each nuclear spin.  $\sigma_d = \pm \frac{1}{2}$  is the electron spin state.  $c(t) = \pm 1$  describes a function that switches its sign whenever a  $\pi$ -pulse is applied, i.e. switches from  $+1$  to  $-1$  after half of the evolution time for a spin echo. The initial configuration of the transverse Overhauser field components is determined by  $b_{k,d}(0) \in \mathbb{C}$ . After the first two evolutions, this initial state has evolved to

$$b_{k,d}^\sigma(t_1 + \tau) = b_k(0) \begin{cases} e^{i\omega_k(t_1 + \tau)} e^{i\sigma A_k \tau} & \text{FID} \\ e^{i\omega_k(t_1 + \tau)} & \text{SE,} \end{cases} \quad (12.20)$$

depending on whether the second evolution was a free induction decay or spin echo experiment, i.e. whether a  $\pi$ -pulse was applied at  $\frac{\tau}{2}$  or not. Indeed, the backaction from the electron spin cancels out for the intermediate spin echo whereas the free induction decay leads to an additional term stemming from this interaction.

The phases determining the measurement outcomes can be written as

$$\begin{aligned}\phi_{d,\sigma} &= \frac{g\mu_B}{4|B_{ext}|} \sum_{k,l} b_k(0)b_l^*(0) \sum_{\sigma=\pm 1} \int_0^{t_1} dt' c(t') e^{i\omega_{kl}t' + i\sigma A_{kl} \int_0^{t_1} dt'' c(t'')} \\ \phi'_{d,\sigma} &= \frac{g\mu_B}{4|B_{ext}|} \sum_{k,l} b_k^\sigma(t_1 + \tau) b_l^{\sigma*}(t_1 + \tau) \sum_{\sigma=\pm 1} \int_0^{t_2} dt' c(t') e^{i\omega_{kl}t' + i\sigma A_{kl} \int_0^{t_2} dt'' c(t'')},\end{aligned}\quad (12.21)$$

where  $\omega_{kl} = \omega_k - \omega_l$  denotes the relative Larmor frequencies of  $b_k^\sigma(t)$  and  $b_l^\sigma(t)$  and  $A_{kl} = A_k - A_l$  is their relative hyperfine coupling. The subscript  $d = L, R$  denotes the dot (left and right) and has been suppressed on the RHS. The sum over the two electron spin states is due to the initialization into a superposition state. Note that the phase of the initial Overhauser field configuration of the third evolution is determined by the first two evolutions of duration  $t_1$  and  $\tau$ , respectively, and thus includes possible backaction on the nuclear spin bath during the intermediate evolution. Plugging these phases into the expectation values of Eq. 12.18 under the assumption of  $t_1 = t_2 = t$  leads to

$$\left\langle e^{i(\phi_{d,\sigma} \pm \phi'_{d,\sigma})} \right\rangle = \left\langle e^{-\frac{i}{2} \sum_{k,l} T_{kl,d}^{\pm\sigma} z_k z_l^*} \right\rangle \quad (12.22)$$

where

$$T_{kl,d}^{\pm,\sigma} = \frac{4ig\mu_B \bar{b}_k \bar{b}_l \exp(i\frac{\omega_{kl}}{2}t)}{\hbar|B_{ext}| i\omega_{kl}} \sin^2\left(\frac{\omega_{kl}}{4}t\right) \cdot \begin{cases} \left(1 \pm e^{i\omega_{kl}(t+\tau)} e^{i\sigma A_{kl}\tau}\right) & \text{FID} \\ \left(1 \pm e^{i\omega_{kl}(t+\tau)}\right) & \text{SE} \end{cases}, \quad (12.23)$$

is a  $n \times n$  matrix similar to that of Ref. [50]. The initial transverse Overhauser field  $b_k(0) = \bar{b}_k z_k$  with  $z_k \in \mathbb{C}$  have been expressed as random Gaussian variables and the rms Overhauser field components  $\bar{b}_k = \frac{\hbar A_k}{g\mu_B} \sqrt{\frac{N_k a_k}{2}}$  with  $a_k = \frac{2}{3}(I_k + 1)I_k = \frac{5}{2}$  analogous to Ref. [71]. Averaging over the Gaussian random variables  $z_k$  leads to

$$\left\langle e^{i(\phi_{d,\sigma} \pm \phi'_{d,\sigma})} \right\rangle = \prod_m \frac{1}{1 + i\lambda_{m,d}^{\pm,\sigma}} \quad (12.24)$$

where  $\{\lambda_{m,d}^{\pm,\sigma}\}$  are the eigenvalues of the  $n \times n$  matrix  $T_d^{\pm,\sigma}$ . To calculate the correlation function, it is necessary to take into account that the electron spin in each dot is in a superposition state during the intermediate evolution. Hence, also the Overhauser field components are projected into a superposition due to the backaction from the electron spin. Under the assumption that in an experiment one would typically average over many

runs of the scheme and thus be unable to distinguish a superposition state from a mixed state, I include this effect by averaging over the two intermediate electron spin states  $|\uparrow\rangle$  and  $|\downarrow\rangle$ , corresponding to  $\sigma = \pm$ . Eq. 12.18 is then modified to

$$\begin{aligned} \langle C \rangle &= \frac{1}{4} \Re \left[ \langle e^{i(\phi_{L,\uparrow} + \phi_{L,\uparrow'})} \rangle \langle e^{-i(\phi_{R,\downarrow} + \phi'_{R,\downarrow})} \rangle + \langle e^{i(\phi_{L,\downarrow} + \phi'_{L,\downarrow})} \rangle \langle e^{-i(\phi_{R,\uparrow} + \phi'_{R,\uparrow})} \rangle \right] \\ &+ \frac{1}{4} \Re \left[ \langle e^{i(\phi_{L,\uparrow} - \phi'_{L,\uparrow})} \rangle \langle e^{-i(\phi_{R,\downarrow} - \phi'_{R,\downarrow})} \rangle + \langle e^{i(\phi_{L,\downarrow} - \phi'_{L,\downarrow})} \rangle \langle e^{-i(\phi_{R,\uparrow} - \phi'_{R,\uparrow})} \rangle \right]. \end{aligned} \quad (12.25)$$

The calculation of the autocorrelation function with the intermediate free induction decay or spin echo is now possible via the calculation of the eigenvalues of the respective  $T$ -matrix given in Eq. 12.23 and plugging them into Eq. 12.24, leading to

$$\begin{aligned} \langle C \rangle &= \frac{1}{4} \Re \left[ \prod_m \frac{1}{1 + i\lambda_{m,L}^{+\uparrow}} \frac{1}{1 - i\lambda_{m,R}^{+\downarrow}} + \prod_m \frac{1}{1 + i\lambda_{m,L}^{+\downarrow}} \frac{1}{1 - i\lambda_{m,R}^{+\uparrow}} \right] \\ &+ \frac{1}{4} \Re \left[ \prod_m \frac{1}{1 + i\lambda_{m,L}^{-\uparrow}} \frac{1}{1 - i\lambda_{m,R}^{-\downarrow}} + \prod_m \frac{1}{1 + i\lambda_{m,L}^{-\downarrow}} \frac{1}{1 - i\lambda_{m,R}^{-\uparrow}} \right]. \end{aligned} \quad (12.26)$$

If the intermediate evolution contains different elements than the FID and SE considered here, these can be easily implemented via their effect on the nuclear spins in Eq. 12.20. To account for nuclear spin dephasing in the presented model, phenomenological deviations from the nuclear Larmor frequencies  $\delta\omega_k$  with a Gaussian distribution may be included [13].





## Simulations

In this chapter, simulations for the preceding calculations are presented.

### 13.1 Toy model scheme

The autocorrelation functions for the semiclassical and quantum-mechanical calculations in Eq. 12.12 and Eq. 12.16 are illustrated in Fig. 13.1 (a) and (b), respectively, as a function of the intermediate evolution time  $\tau$  and the total number of nuclear spins in each dot  $N$ . The semiclassical approach shows a decay of the autocorrelation function of the two measurements stemming from the intermediate coupling of the electrons to the nuclei in their respective dots. Indeed, this indicates the desired backaction of the electron spin. For  $N \ll 10^4$ , the decay scales with the number of nuclei, similar to the  $T_2^*$  time of a coherence experiment. When  $(A_i \sigma t)^2 \ll 1$  such that the second exponent in Eq. 12.12 is small, the exponential and the sine may be developed to first order leading to

$$\begin{aligned} \langle C \rangle &\approx \frac{1}{2} \prod_{i=1}^N \left( 1 - \int_{-\infty}^{\infty} dJ_i^x \frac{1}{\sqrt{2\pi\sigma^2}} \frac{1}{4} A_i^4 (J_i^x)^2 \tau^2 t^2 e^{-\frac{1}{2} \left( \frac{J_i^x}{\sigma} \right)^2} \right)^2 \\ &= \frac{1}{2} \prod_{i=1}^N \left( 1 - \frac{1}{4} A_i^4 \sigma^4 \tau^2 t^2 \right)^2. \end{aligned} \quad (13.1)$$

Discretization of the hyperfine coupling distribution into  $n$  clusters with  $N_i$  nuclear spins as defined in Eq. 12.6 allows to further simplify this expression to

$$\begin{aligned} \langle C \rangle &= \frac{1}{2} \prod_{i=1}^n \left( 1 - \frac{1}{4} \frac{(A'_i)^4}{N^3} \frac{1}{N_i} \rho(A_i) n_{\alpha[i]} dA \tau^2 t^2 \sigma^4 \right)^{2N_i} \\ &\approx \frac{1}{2} \exp \left( -\frac{1}{2} \sum_{i=1}^n \frac{(A'_i)^4}{N^3} \rho(A_i) n_{\alpha[i]} dA \tau^2 t^2 \sigma^4 \right), \end{aligned} \quad (13.2)$$

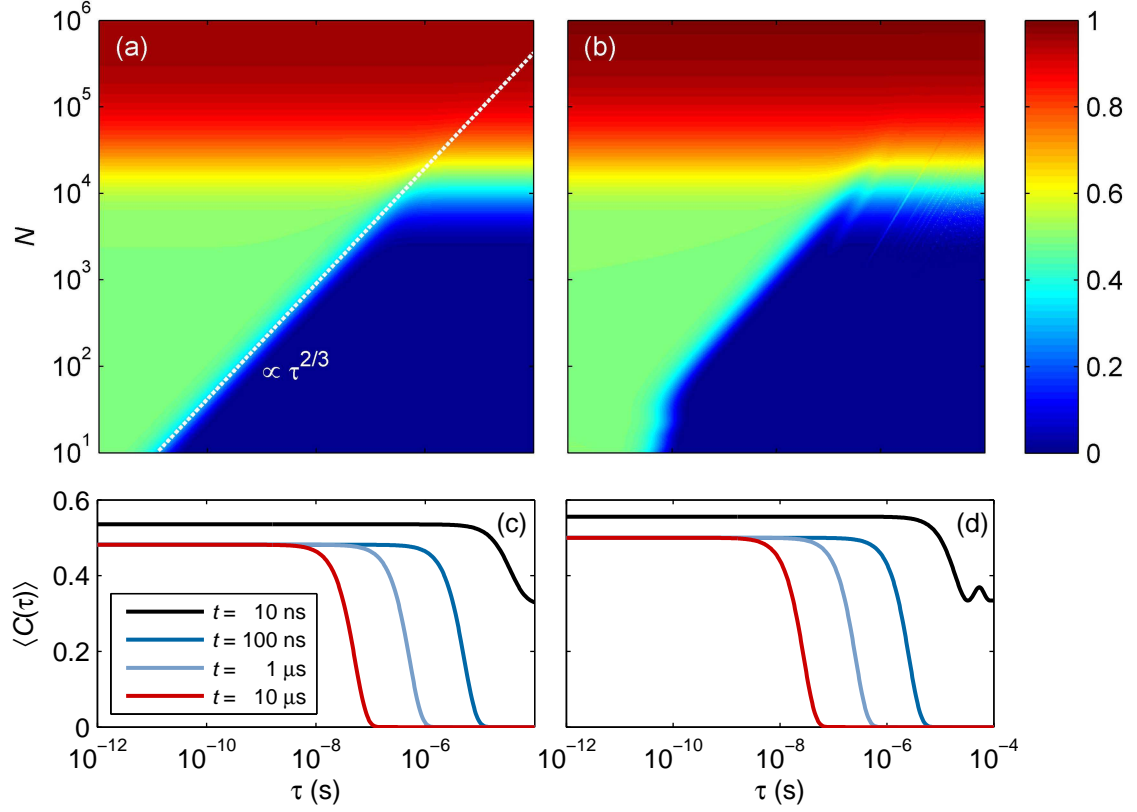


**Figure 13.1:** (a) Autocorrelation function for the semiclassical approach to the toy model scheme shown as colorscale. The intermediate evolution time  $\tau$  and the number of nuclear spins is swept. The evolution time for the two outer evolutions is  $t_1 = t_2 = 1$  ns. The dotted white line denotes where the autocorrelation has decayed to  $\frac{1}{2}e^{-1}$ . For  $N < 10^4$ , the maximum value of  $\langle C \rangle = \frac{1}{2}$  indicates that the first term of Eq. 12.12 is negligible. The change of the power-law behavior for  $N \gtrsim 10^3$  denotes the regime where the hyperfine interaction is negligible. The  $x$ -axis is identical to (c). (b) Same as (a) for the quantum-mechanical approach. The difference from (a) for  $\tau < 0.1$  ns denotes the regime where the semiclassical approach is not valid. The ripples at  $\tau > 1$   $\mu$ s stem from an insufficient discretization of the hyperfine coupling distribution function. (c) Autocorrelation function of the semiclassical approach for different durations of the two outer evolutions.  $t$  acts as a scaling factor determining the position of the decay of correlation. The number of nuclear spins is  $N = 10^6$ , which is the experimentally relevant case for electron spins in GaAs. (d) Same as (c) for the quantum-mechanical calculation. Note the qualitatively different behavior for  $t = 10$  ns. For details see text.

where  $A'_i = N_i \cdot A_i$ . Setting the autocorrelation function to  $\langle C \rangle = \frac{1}{2}e^{-1}$  then leads to

$$N = \left( \frac{1}{2} \sum_{i=1}^n A_i'^4 \rho_\alpha(A_i) n_{\alpha[i]} dA \tau^2 t^2 \sigma^4 \right)^{\frac{1}{3}} \quad (13.3)$$

which indicates the position of the decay illustrated by the white line in Fig. 13.1. For  $N \gtrsim 10^4$  nuclear spins in each dot, the hyperfine coupling is small compared to the outer evolution time  $t$ . In this regime, the outcomes of the two measurements will always be the initialized states leading to a perfect correlation. Comparison with the quantum-

mechanical calculations in Fig. 13.1 (b) shows a similar behavior for  $N > 10^2$ . In this regime, the outer evolution time  $t$  acts as a scaling factor setting the time scale on which the correlation decays. For a smaller number of nuclear spins, the quantum-mechanical calculation reveals deviations from the  $N \propto t^{\frac{2}{3}}$  law of the semiclassical approach. This is due to the strength of the hyperfine coupling on the order of  $t^{-1}$ . The outer evolution time in Eq. 12.14 can thus not be regarded as a simple scaling factor anymore and leads to the nontrivial behavior observed in Fig. 13.1 (b). Variation of the outer evolution time  $t$  shown in Fig. 13.1 (c) and (d) or in colorscale in Fig. 1 (a) and (b) shows a similar effect: Whereas in the semiclassical approach, averaging over the phase, which is similar to an inhomogeneous broadening process, leads to a simple scaling factor  $t$ , the quantum-mechanical calculation reveals that this only holds when the hyperfine coupling is small compared to this duration. The limit  $A_i t \gtrsim 1$  may thus be considered as the regime where the semiclassical approach is insufficient for the calculation of the autocorrelation function. The oscillatory features for  $\tau > 100$  ns in the quantum-mechanical calculation vanish when  $n$  is increased and can thus be attributed to artifacts stemming from an insufficient discretization of the hyperfine coupling distribution.

The simulations indicate that backaction from the electron on the nuclei are indeed detectable with the presented measurement scheme. Under the constraint that the duration of the outer evolutions is short compared to the inverse hyperfine coupling,  $t$  may be used as a scaling factor determining the position of the decay. Tuning this parameter will thus allow to observe the decay of correlation caused solely by the hyperfine interaction between electron and nuclei within a time scale smaller than  $T_2$  which is very beneficial for the experimental observation of backaction effects. The semiclassical model has been shown to accurately reproduce the quantum-mechanical calculations for nuclear spin baths as small as 100 spins, which shows that the semiclassical model can indeed be used to calculate the quantum-mechanical hyperfine interaction for the experimentally relevant cases e.g. InGaAs with typically  $N = 10^4$  or GaAs with a nuclear spin bath consisting of  $10^6$  spins.

## 13.2 Pulse scheme

In the previous chapter, the backaction has been shown to lead to a detectable effect via readout of the autocorrelation function for the toy model measurement scheme. In this chapter, simulations are presented that aim at detecting backaction with the pulse scheme. In Fig. 13.2, the autocorrelation function given by Eq. 12.26 is shown as a function of the intermediate evolution time  $\tau$  and the outer evolution time  $t$  with an applied external magnetic field of  $B_{ext} = 30$  mT. The relative phases of the transverse Overhauser field components lead to revivals of the correlation as a function of  $\tau$ . The conditions for a revival of the first term in Eq. 12.26 is  $\omega_{kl}(\tau + t) = (2n + 1)\pi$  whereas the second

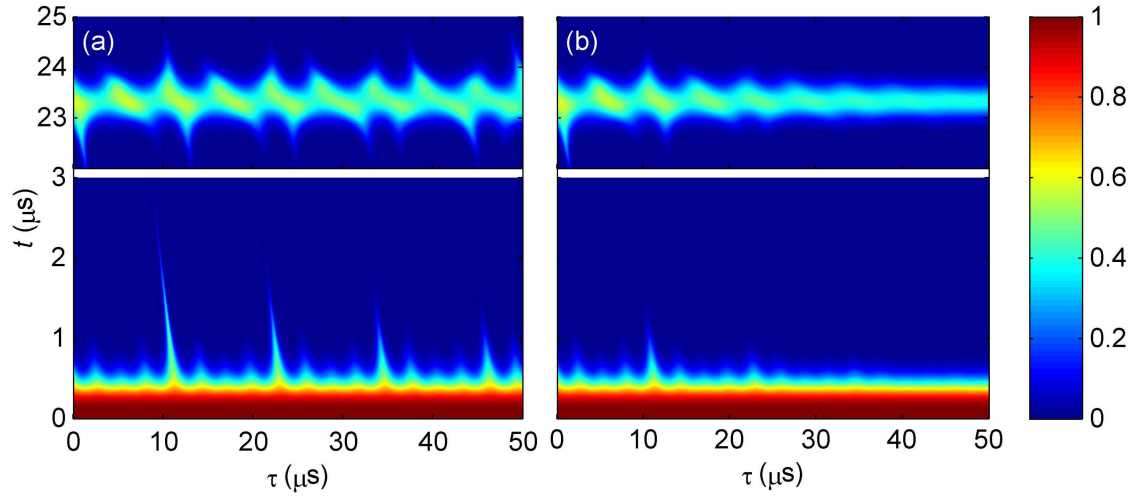


**Figure 13.2:** (a) Autocorrelation function in colorscale for the pulse scheme with intermediate spin echo evolution as a function of the intermediate evolution time  $\tau$  and the outer evolution times  $t$ . The applied external magnetic field is 30 mT and the number of nuclei is  $N = 10^6$ . The correlation exhibits clear revivals at the relative Larmor frequencies both as a function of the intermediate evolution time  $\tau$  and the outer evolution times  $t$ . Note the separated  $t$ -scale. The peaks are tilted due to oscillations with time  $t + \tau$  in Eq. 12.23. (b) Same as (a) with an intermediate free induction decay. Due to the backaction from the electron spin, the Larmor revivals vanish.

term has revivals whenever  $\omega_{kl}(\tau + t) = 2n\pi$  where  $n$  is an integer. These conditions can be derived from Eq. 12.23. The fortuitous spacing of the Larmor frequencies ensures the commensurability of the three  $\omega_{kl}$ , allowing to fulfill the revival condition for all relative frequencies. This corresponds to a realignment of the transverse Overhauser field components. The smaller peaks indicate conditions where not all three spin species are aligned. The revivals are shifted due to oscillations with  $\tau + t$ . Analog to a spin echo experiment, at  $\omega_{kl}\frac{t}{2} = 2n\pi$  another band with a high correlation appears due to the term oscillating with  $\frac{\omega_{kl}}{4}t$  in Eq. 12.23. This band corresponds to a refocussing of the Overhauser field components of all three nuclear spin species in the middle of the two outer evolutions, which is necessary due to the application of the  $\pi$ -pulse at this point. In these bands, the precession of the transverse Overhauser field components is such that the two measurements always measure the initialized state, resulting in a perfect correlation. In Fig. 13.2 (a), a  $\pi$ -pulse is applied during the intermediate evolution, effectively reversing any backaction from the electron spin during the measurement cycle. Turning on the backaction from the electron spin on the nuclei with an intermediate FID is depicted in Fig. 13.2 (b) and leads to a strong suppression of the revival behavior. Note that this behavior stems solely from the backaction as all other parameters are identical to (a). The effect of the backaction thus manifests itself in a suppression of the Larmor frequency revivals due to a smearing out of the phase. Variation of the magnetic field is depicted

in Fig. 13.3 and shows a qualitatively similar behavior: for an intermediate spin echo, Larmor revivals are observed whereas under the influence of backaction, they are strongly suppressed. Variation of the magnetic field changes the time scale of the revivals. Note

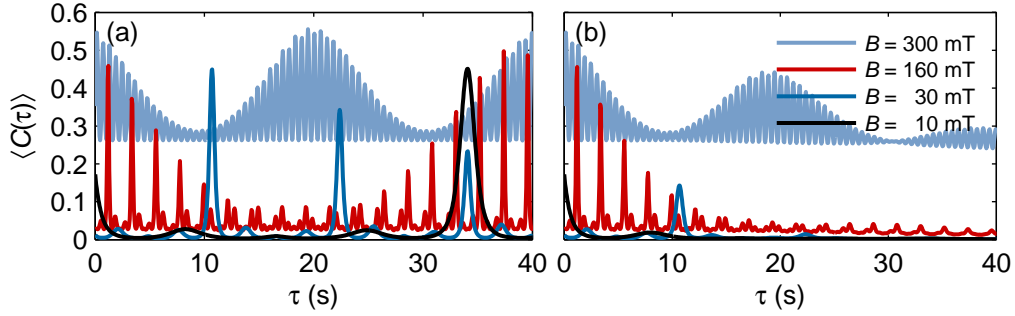


**Figure 13.3:** (a) Autocorrelation function for the pulse scheme with intermediate spin echo evolution as a function of the intermediate evolution time  $\tau$ . The outer evolution time is  $t = 1 \mu\text{s}$ . The black, dark blue, red and light blue curve illustrate the correlation for an external field of 10, 30, 160 and 300 mT, respectively. The external magnetic field sets the relative Larmor frequencies and thus the time scale of the correlation revivals. The number of nuclei is  $N = 10^6$ . (b) Same as (a) with an intermediate free induction decay. Under the influence of the backaction from the electron spin, the revivals disappear.

that for the curve corresponding to an external field of 10 and 30 mT, respectively, the first and third revival coincide. For large magnetic fields, the revivals are pronounced less strong as the correlation does not decay to 0. Further increase of  $B_{ext}$  will thus lead to oscillation amplitudes below the signal-to-noise level. In Fig. 2 and 3 in the Appendix, the correlation is shown as colorscale analog to Fig. 13.2 for 160 and 300 mT, respectively. The revivals in the simulations are equivalent to those observed in Ref. [13]. In these experiments, 4-5 revivals were resolvable on a time scale similar to that of the simulations above. I thus expect that the pulse scheme will lead to a well measurable backaction effect under experimental conditions as the interaction of the nuclear spin bath with the electron spin suppresses the revival behavior already at the first revival, as shown in Fig. 13.2. Switching the fast  $\pi$ -pulse on and off during the intermediate evolution and observation of the resulting effect on the correlation will thus reveal the electron spin backaction while maintaining all other experimental parameters constant.



## Summary

In this part, I have presented two measurement schemes to detect backaction from an electron spin qubit coupled to a nuclear spin bath via correlations of noncommuting measurements. For the toy model scheme, a semiclassical and a quantum-mechanical approach to calculate the autocorrelation function was employed. For experimentally realistic parameters, the semiclassical approach accurately reproduced the quantum-mechanical calculations for evolution times smaller than the inverse coupling energy of the electron to the nuclei. Simulations for the toy model scheme were presented that showed a measurable backaction on time scales smaller than the qubit dephasing time. However, the experimental requirement of a fast rotation of the external magnetic field is infeasible to fulfill. The calculations and simulations for this scheme thus rather serve as a simple example to illustrate the detection of backaction on the nuclear spin bath via correlations of noncommuting measurements.

For the pulse scheme, which relied on the optional application of a  $\pi$ -pulse during an intermediate evolution time, a theoretical model similar to that of Ref. [71] was employed. The simulations exhibited revivals in the correlation function stemming from the Larmor precessions of the transverse Overhauser field components composed by the different nuclear spin species. Effectively turning on and off the backaction from the electron spin via the optional application of a  $\pi$ -pulse during the intermediate evolution led to a strong suppression of the revivals caused by the backaction on the nuclear spins. Due to the strength of this suppression, I expect this effect to be well measurable and thus clearly show a resolvable backaction in the singlet triplet qubit. Moreover, the outer evolution times and the external magnetic field may be chosen such that the backaction effect is detectable on a time scale smaller than  $T_2$  which is beneficial for the experiment. Note that the results are easily applicable to a single electron and lead to similar results in this case. Though the simulations were performed with parameters for electron spins in a GaAs lattice, other material such as InGaAs may be included easily via adjustment of the parameters in Tab. 10.1.





## Part IV

---

### Conclusion



## Conclusion

In this thesis, interactions between a qubit and the surrounding noise bath were investigated. Techniques to study the bath properties via correlations of projective qubit readout were introduced and simulations exhibiting the usefulness of these methods were presented. The only experimental requirements assumed are that initialization, application of a  $\pi$ -pulse and projective measurement of the qubit are faster than typical evolution times. Furthermore, initialization may be replaced by measurement such that the only requirement is a fast single-shot readout and short  $\pi$ -pulses, which is experimentally well feasible for the qubits systems based on electron spins and superconducting circuits considered here.

In Part II, a classical noise bath coupled to a quantum-mechanical two-level system was considered. The presented measurement scheme consisted of correlating two initialization-evolution-measurement cycles and has been shown to extract properties of the noise bath spectrum over an extremely large frequency range expanding over more than four orders of magnitude. The ability to control the duration of the two pulses and their temporal spacing allows to tailor both the magnitude and position of the technique's sensitivity as required. Simulations based on experimental parameters strongly indicate that this scheme might also be used for the investigation of frequency regions between direct and pulse sequence-based spectroscopy. I thus assume that the presented technique will outperform existing techniques also due to the ease of experimental implementation in stark contrast to the application of numerous  $\pi$ -pulses necessary to investigate low frequencies with pulse sequence-based spectroscopy. The technique will thus be of great aid for the investigation of the potential extension of the  $1/f^\alpha$  behavior over the whole frequency range in superconducting qubits, and also the assumed suppression of nuclear spin diffusion for short correlation times in electron spin qubits. Note, however, that the measurement scheme and the calculations are general with respect to the qubit system as long as the requirement of fast single-shot measurement is fulfilled.

In Part III, the coupling of an electron spin to a quantum-mechanical nuclear spin bath was considered. Taking into account quantum-mechanical interactions from the electron spin on the nuclear spins was motivated by the question whether the noise bath shows

measurable quantum-mechanical behavior such that the assumption of a classical bath is invalid. Due to the large number of nuclear spins, this question relates to investigations of quantum-mechanical behavior in macroscopic systems. In order to detect backaction from the electron on the nuclear spins, i.e. electron spin-dependent nuclear spin dynamics in this system, two different measurement schemes were presented that relied on the implementation of noncommuting measurements. The first scheme was based on the rotation of the externally applied magnetic field to effectively rotate the quantization axis of the electron. As this approach is experimentally infeasible due to the required fast rotation, the scheme served as a simple example. A semiclassical and a quantum-mechanical model was employed to calculate the autocorrelation function. For evolution times large compared to the hyperfine coupling between the electron and nuclei, the semiclassical calculation reproduced the quantum-mechanical simulations and exhibited a decay of correlation solely due to backaction. As the first measurement of the scheme projects each nuclear spin into a superposition state, the decay of correlation is linked to the quantum-mechanical properties of each nuclear spin. Appropriate choice of the evolution times allowed to set the time scale of the decay such that it is faster than the electron dephasing time and thus in principle well detectable.

In the second scheme, correlations of two spin echo experiments framing an intermediate evolution with an optional  $\pi$ -pulse were considered. The application of the pulse allowed to reverse any backaction whereas in its absence the electron affected the nuclear spin dynamics. Comparison of simulations for both cases showed a strong suppression of revivals stemming from the Larmor precessions of the nuclei if the backaction is present. As those Larmor revivals have already been observed, I expect this scheme to lead to a well measurable backaction in experiments. The implementation of the scheme will thus reveal whether the quantum-mechanical behavior of the nuclear spin bath predicted in the simulations is also detectable experimentally. If so, this indicates that even a spin bath as large as  $10^6$  spins shows effects that necessitate a quantum-mechanical description. To further improve the presented model, nuclear spin dephasing may be included via local Larmor frequency shifts.

The calculations performed are general in the sense that they can easily be applied to any other system composed of a single spin coupled to a bath of other spins. Moreover, the calculations for the toy model scheme set up a framework that may be used for the calculation of the autocorrelation of two evolutions with an arbitrary unitary evolution in between.

---

## Appendix

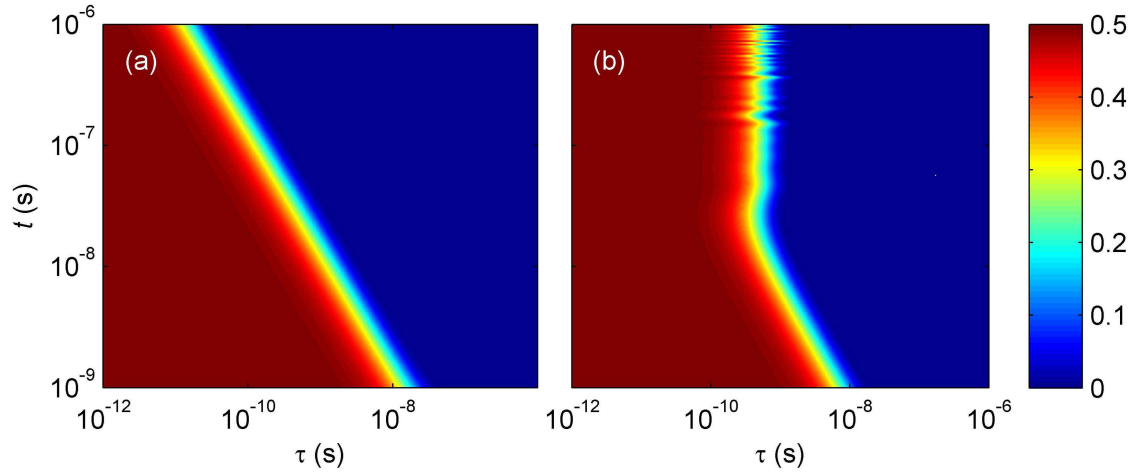


**Figure 1:** (a) Autocorrelation function for the semiclassical approach to the toy model scheme shown as colorscale. The intermediate evolution time  $\tau$  and the duration of the outer evolutions  $t$  is swept. The number of nuclear spins is  $N = 10^3$ .  $t$  acts as a scaling factor effectively shifting the position of the decay of correlation with respect to  $\tau$ . (b) Same as (a) for the quantum-mechanical approach. For  $t < 10$  ns, the autocorrelation is equivalent to the semiclassical calculation. For  $t \gtrsim 50$  ns, however, the behavior is qualitatively different: The decay does not shift its position with respect to  $\tau$  when  $t$  is increased. This is due to  $A_i t \gtrsim 1$  in this regime such that  $t$  can not be regarded as a scaling factor in Eq. 12.14 but leads to the oscillatory behavior.

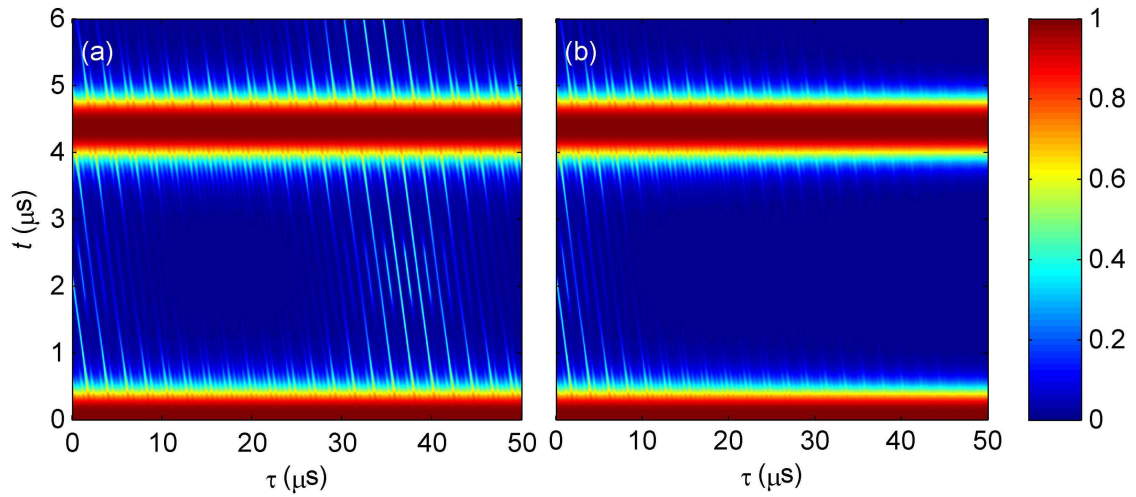


**Figure 2:** (a) Autocorrelation function in colorscale for the pulse scheme with intermediate spin echo evolution as a function of the intermediate evolution time  $\tau$  and the outer evolution times  $t$ . The applied external magnetic field is 160 mT and the number of nuclei is  $N = 10^6$ . The correlation exhibits revivals at the relative Larmor frequencies as a function of the intermediate evolution time  $\tau$ . The peaks are tilted due to oscillations with time  $t + \tau$  in Eq. 12.23. (b) Same as (a) with an intermediate free induction decay. Due to the backaction from the electron spin, the Larmor revivals vanish.

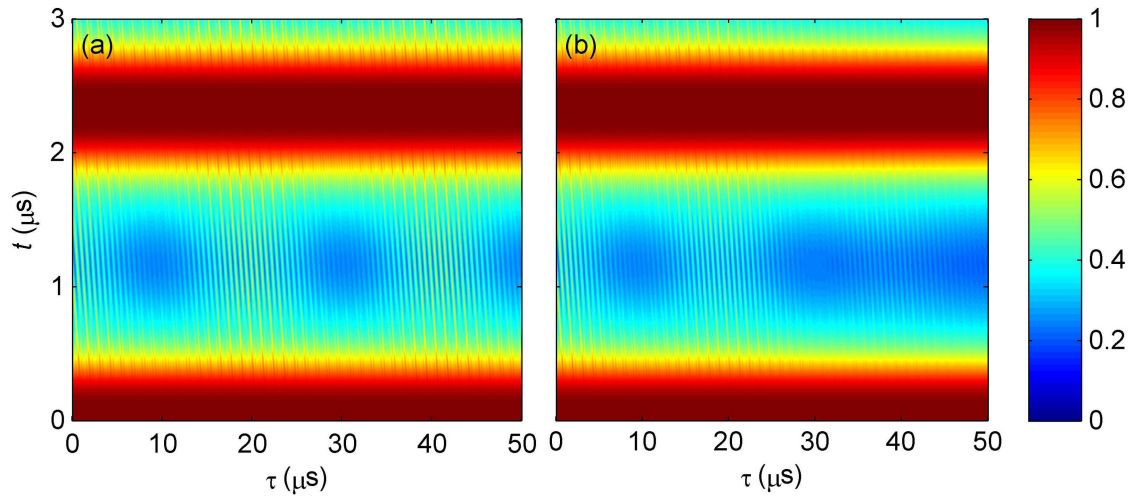


**Figure 3:** (a) Same as Fig. 2 for  $B_{ext} = 300$  mT. The revivals are not clearly pronounced anymore due to the large magnetic field and only decrease to  $\langle C \rangle \sim 0.3$ . Further increase of the external magnetic field will thus lead to oscillations that are not resolvable anymore (b) Same as (a) with an intermediate free induction decay.

---

# Bibliography

- [1] I. Georgescu, *Nature Physics* **8**, 777 (2012). Cited on page 3.
- [2] S. Lloyd, *Science* **319**, 1209 (2008). Cited on page 3.
- [3] I. Buluta and F. Nori, *Science* **326**, 108 (2009). Cited on page 3.
- [4] R. P. Feynman, *International Journal of Theoretical Physics* **21**, 467 (1982). Cited on page 3.
- [5] A. Trabesinger, *Nature Physics* **8**, 263 (2012). Cited on page 3.
- [6] P. Shor, in *Foundations of Computer Science, 1994 Proceedings., 35th Annual Symposium on* (1994), pp. 124–134. Cited on page 3.
- [7] L. K. Grover, in *Proceedings of the twenty-eighth annual ACM symposium on Theory of computing* (1996), STOC '96, pp. 212–219. Cited on page 3.
- [8] A. W. Harrow, A. Hassidim, and S. Lloyd, *Physical Review Letters* **103**, 150502 (2009). Cited on page 3.
- [9] M. A. Nielsen and I. L. Chuang, *Quantum Computation and Quantum Information - 10th Anniversary Edition* (Cambridge University Press, 2010), ISBN 978-1-107-00217-3. Cited on page 5.
- [10] D. P. DiVincenzo and D. Loss, *Superlattices and Microstructures* **23**, 419 (1998). Cited on page 5.
- [11] D. P. DiVincenzo, *Fortschritte der Physik* **48**, 771 (2000). Cited on page 5.
- [12] J. R. Petta, A. C. Johnson, J. M. Taylor, E. A. Laird, A. Yacoby, M. D. Lukin, C. M. Marcus, M. P. Hanson, and A. C. Gossard, *Science* **309**, 2180 (2005). Cited on pages 7, 19, 35, and 58.
- [13] H. Bluhm, S. Foletti, I. Neder, M. Rudner, D. Mahalu, V. Umansky, and A. Yacoby, *Nature Physics* **7**, 109 (2010). Cited on pages 7, 15, 34, 46, 50, 57, 65, and 71.
- [14] J. M. Taylor, J. R. Petta, A. C. Johnson, A. Yacoby, C. M. Marcus, and M. D. Lukin, *Physical Review B* **76**, 035315 (2007). Cited on page 9.

- [15] C. Barthel, M. Kjærgaard, J. Medford, M. Stopa, C. M. Marcus, M. P. Hanson, and A. C. Gossard, *Physical Review B* **81**, 161308 (2010). Cited on pages 9 and 23.
- [16] C. Barthel, D. J. Reilly, C. M. Marcus, M. P. Hanson, and A. C. Gossard, *Physical Review Letters* **103**, 160503 (2009). Cited on page 9.
- [17] J. M. Elzerman, R. Hanson, L. H. W. van Beveren, B. Witkamp, L. M. K. Vandersypen, and L. P. Kouwenhoven, *Nature* **430**, 431 (2004). Cited on page 9.
- [18] M. Büttiker, *Physical Review B* **36**, 3548 (1987). Cited on page 9.
- [19] V. Bouchiat, D. Vion, P. Joyez, D. Esteve, and M. H. Devoret, *Physica Scripta* **1998**, 165 (1998).
- [20] Y. Nakamura, Y. Pashkin, and J. Tsai, *Nature* **398**, 786 (1999). Cited on page 9.
- [21] M. l. Devoret and J. M. Martinis, *Quantum Information Processing* **3**, 163 (2004). Cited on page 9.
- [22] J. M. Martinis, *Quantum Information Processing* **8**, 81 (2009). Cited on page 9.
- [23] D. Ristè, J. G. van Leeuwen, H.-S. Ku, K. W. Lehnert, and L. DiCarlo, *Physical Review Letters* **109**, 050507 (2012). Cited on pages 9 and 23.
- [24] J. Koch, T. M. Yu, J. Gambetta, A. A. Houck, D. I. Schuster, J. Majer, A. Blais, M. H. Devoret, S. M. Girvin, and R. J. Schoelkopf, *Physical Review A* **76**, 042319 (2007). Cited on pages 9 and 10.
- [25] B. D. Josephson, *Review of Modern Physics* **36**, 216 (1964). Cited on page 9.
- [26] A. Fedorov, L. Steffen, M. Baur, M. P. da Silva, and A. Wallraff, *Nature* **481**, 170 (2012). Cited on page 9.
- [27] E. Lucero, R. Barends, Y. Chen, J. Kelly, M. Mariantoni, A. Megrant, P. O'Malley, D. Sank, A. Vainsencher, J. Wenner, et al., *Nature Physics* **8**, 719 (2012). Cited on page 10.
- [28] C. P. Slichter, *Principles of magnetic resonance* (Springer-Verlag, 1990), ISBN 978-3-540-50157-2. Cited on page 10.
- [29] D. J. Reilly, J. M. Taylor, E. A. Laird, J. R. Petta, C. M. Marcus, M. P. Hanson, and A. C. Gossard, *Physical Review Letters* **101**, 236803 (2008). Cited on pages 10, 16, 17, and 24.
- [30] S. Amasha, K. MacLean, I. P. Radu, D. Zumbühl, M. Kastner, M. P. Hanson, and A. C. Gossard, *Physical Review Letters* **100**, 046803 (2008). Cited on pages 10 and 17.



- [31] J. Bylander, S. Gustavsson, F. Yan, F. Yoshihara, K. Harrabi, G. Fitch, D. G. Cory, Y. Nakamura, J.-S. Tsai, and W. D. Oliver, *Nature Physics* **7**, 565 (2011). Cited on pages [10](#), [15](#), [17](#), [20](#), [21](#), [38](#), and [41](#).
- [32] Y. Nakamura, Y. Pashkin, T. Yamamoto, and J.-S. Tsai, *Physical Review Letters* **88**, 047901 (2002).
- [33] F. Yoshihara, K. Harrabi, A. Niskanen, Y. Nakamura, and J.-S. Tsai, *Physical Review Letters* **97**, 167001 (2006). Cited on page [20](#).
- [34] K. Kakuyanagi, T. Meno, S. Saito, H. Nakano, K. Semba, H. Takayanagi, F. Deppe, and A. Shnirman, *Physical Review Letters* **98**, 047004 (2007). Cited on pages [10](#) and [17](#).
- [35] E. L. Hahn, *Physical Review* **80**, 580 (1950). Cited on page [11](#).
- [36] S. Meiboom and D. Gill, *Review of Scientific Instruments* **29**, 688 (1958). Cited on page [11](#).
- [37] K. Khodjasteh and D. A. Lidar, *Physical Review A* **75**, 062310 (2007). Cited on page [11](#).
- [38] G. Uhrig, *Physical Review Letters* **98**, 100504 (2007). Cited on page [11](#).
- [39] W. Yao, R.-B. Liu, and L. J. Sham, *Physical Review B* **74**, 195301 (2006). Cited on pages [15](#), [48](#), and [53](#).
- [40] L. Cywiński, R. Lutchyn, C. Nave, and S. Das Sarma, *Physical Review B* **77**, 174509 (2008). Cited on pages [15](#), [17](#), [26](#), and [27](#).
- [41] T. Yuge, S. Sasaki, and Y. Hirayama, *Physical Review Letters* **107**, 170504 (2011). Cited on page [15](#).
- [42] R. Bialczak, R. McDermott, M. Ansmann, M. Hofheinz, N. Katz, E. Lucero, M. Neeley, A. O'Connell, H. Wang, A. Cleland, et al., *Physical Review Letters* **99**, 187006 (2007). Cited on pages [16](#), [20](#), and [24](#).
- [43] D. Sank, R. Barends, R. C. Bialczak, Y. Chen, J. Kelly, M. Lenander, E. Lucero, M. Mariantoni, A. Megrant, M. Neeley, et al., *Physical Review Letters* **109**, 067001 (2012). Cited on pages [16](#) and [20](#).
- [44] G. de Lange, T. van der Sar, M. Blok, Z.-H. Wang, V. Dobrovitski, and R. Hanson, *Scientific Reports* **2**, 382 (2012). Cited on page [16](#).
- [45] F. Yan, J. Bylander, S. Gustavsson, F. Yoshihara, K. Harrabi, D. G. Cory, T. P. Orlando, Y. Nakamura, J.-S. Tsai, and W. D. Oliver, *Physical Review B* **85**, 174521 (2012). Cited on pages [16](#), [20](#), and [24](#).

- [46] K. C. Young and K. B. Whaley, *Physical Review A* **86**, 012314 (2012). Cited on page [16](#).
- [47] M. Biercuk and H. Bluhm, *Physical Review B* **83**, 235316 (2011). Cited on pages [16](#), [19](#), [20](#), and [34](#).
- [48] T. Fink and H. Bluhm, *Physical Review Letters* **110**, 010403 (2013). Cited on page [16](#).
- [49] A. Johnson, J. Petta, J. Taylor, A. Yacoby, M. Lukin, C. Marcus, M. Hanson, and A. Gossard, *Nature* **435**, 925 (2005). Cited on pages [18](#) and [19](#).
- [50] L. Cywiński, W. M. Witzel, and S. Das Sarma, *Physical Review B* **79**, 245314 (2009). Cited on pages [18](#), [48](#), [49](#), [52](#), [57](#), [58](#), and [64](#).
- [51] C. Latta, A. Srivastava, and A. Imamoglu, *Physical Review Letters* **107**, 167401 (2011). Cited on page [19](#).
- [52] F. C. Wellstood, C. Urbina, and J. Clarke, *Applied Physics Letters* **50**, 772 (1987). Cited on page [20](#).
- [53] G. Ithier, E. Collin, P. Joyez, P. J. Meeson, D. Vion, D. Esteve, F. Chiarello, A. Shnirman, Y. Makhlin, J. Schrieffer, et al., *Physical Review B* **72**, 134519 (2005). Cited on page [20](#).
- [54] L. Faoro and L. B. Ioffe, *Physical Review Letters* **100**, 227005 (2008). Cited on page [20](#).
- [55] P. Dutta and P. M. Horn, *Review of Modern Physics* **53**, 497 (1981). Cited on page [21](#).
- [56] P. Bak, C. Tang, and K. Wiesenfeld, *Physical Review Letters* **59**, 381 (1987). Cited on page [21](#).
- [57] R. Kubo, *Journal of the Physical Society of Japan* **17**, 1100 (1962). Cited on page [26](#).
- [58] R. Corless, G. Gonnet, D. Hare, D. Jeffrey, and D. Knuth, *Advances in Computational Mathematics* **5**, 329 (1996). Cited on page [38](#).
- [59] M. Arndt, O. Nairz, J. Vos-Andreae, C. Keller, G. van der Zouw, and A. Zeilinger, *Nature* **401**, 680 (1999). Cited on page [45](#).
- [60] A. J. Leggett, *Journal of Physics: Condensed Matter* **14**, R415 (2002). Cited on page [45](#).
- [61] B. Herzog and E. L. Hahn, *Physical Review* **103**, 148 (1956). Cited on page [47](#).

- [62] A. M. Portis, *Physical Review* **104**, 584 (1956).
- [63] G. Feher and E. A. Gere, *Physical Review* **114**, 1245 (1959).
- [64] W. B. Mims, K. Nassau, and J. D. McGee, *Physical Review* **123**, 2059 (1961).
- [65] J. R. Klauder and P. W. Anderson, *Physical Review* **125**, 912 (1962).
- [66] M. Chiba and A. Hirai, *Journal of the Physical Society of Japan* **33**, 730 (1972).  
Cited on page [47](#).
- [67] L. Cywiński, W. M. Witzel, and S. Das Sarma, *Physical Review Letters* **102**, 057601 (2009). Cited on page [48](#).
- [68] L. Cywiński, V. V. Dobrovitski, and S. Das Sarma, *Physical Review B* **82**, 035315 (2010). Cited on page [48](#).
- [69] S. K. Saikin, W. Yao, and L. J. Sham, *Physical Review B* **75**, 125314 (2007). Cited on page [48](#).
- [70] W. Yao, R.-B. Liu, and L. J. Sham, *Physical Review Letters* **98**, 077602 (2007). Cited on page [48](#).
- [71] I. Neder, M. S. Rudner, H. Bluhm, S. Foletti, B. I. Halperin, and A. Yacoby, *Physical Review B* **84**, 035441 (2011). Cited on pages [49](#), [50](#), [55](#), [57](#), [63](#), [64](#), and [73](#).
- [72] K. M. Weiss, J. M. Elzerman, Y. L. Delley, J. Miguel-Sanchez, and A. Imamoglu, *Physical Review Letters* **109**, 107401 (2012). Cited on page [58](#).



---

# List of Figures

2.1	Bloch sphere . . . . .	6
2.2	Singlet triplet qubit . . . . .	7
2.3	Energy diagram of a singlet triplet qubit . . . . .	8
2.4	Schematic representation of superconducting qubits . . . . .	10
2.5	Coherence times . . . . .	11
2.6	Spin echo sequence . . . . .	12
4.1	Schematic of hyperfine coupling in singlet triplet qubit . . . . .	18
4.2	Overhauser field fluctuation noise spectral density . . . . .	20
5.1	Measurement scheme . . . . .	23
6.1	Filter function of the autocorrelation function . . . . .	29
7.1	Autocorrelation for a Lorentzian spectrum . . . . .	32
7.2	Autocorrelation for a double Lorentzian spectrum . . . . .	34
7.3	Autocorrelation for nuclear spin diffusion with exponential cutoff . . . . .	35
7.4	$-\chi_-(\tau, \Delta t)/2$ with high-frequency cutoff . . . . .	36
7.5	Autocorrelation for the nuclear spin diffusion spectrum . . . . .	37
7.6	Autocorrelation for $1/f^\alpha$ noise with varying evolution time . . . . .	39
10.1	Illustration of the central spin problem . . . . .	48
11.1	Measurement sequence for the toy model scheme . . . . .	54
11.2	Measurement sequence for the pulse scheme . . . . .	55
12.1	Distribution of hyperfine couplings . . . . .	59
13.1	Autocorrelation for the toy model scheme . . . . .	68
13.2	Autocorrelation for the pulse scheme at 30 mT . . . . .	70
13.3	Autocorrelation for the pulse scheme at various external fields . . . . .	71
1	Autocorrelation for the toy model scheme . . . . .	I
2	Autocorrelation for the pulse scheme at 160 mT . . . . .	II
3	Autocorrelation for the pulse scheme at 300 mT . . . . .	II



---

# Acknowledgements

The work in this thesis benefited from interactions with many people. First of all, I would like to thank my advisor Hendrik Bluhm for giving me the opportunity to work in his group on this highly interesting subject. I am indebted to him for his guidance, his support both in my research and also my academic development, and his persistent willingness to discuss arising problems. His intuition-based way of thinking has taught me a lot about how to approach physics.

I thank Barbara Terhal for co-supervising my thesis.

Especially in the beginning of this thesis, I profited very much from conversations with Tim Botzem, Jan-Michael Mol, Lars Schreiber, and Rob McNeil. Thank you for patiently explaining what was unclear to me and for discussing ideas and arising issues.

Thank you Tim Botzem and Pascal Cerfontaine for proofreading this thesis and in particular Rob McNeil for never getting tired of working through my drafts.

I would like to thank everyone in the group for the open and warm atmosphere that always made me look forward to come to the office. I very much enjoyed conversations, discussions, group activities, and lunchtimes as well as our infamous post-lunch-stress-relief-technique.

I am very thankful for having such a close-knit and sympathetic family that unconditionally supports me in all my endeavors. Thank you for enabling me to follow my interests.

Thank you Franziska for your support.





---

# Statement of authorship

I hereby declare that this document has been composed by myself and describes my own work, unless otherwise acknowledged in the text. It has not been accepted in any previous application for a degree. All sources of information have been specifically acknowledged in all conscience.

---

Aachen, December 31, 2012 Thomas Fink